

Fast-charging aluminium–chalcogen batteries resistant to dendritic shorting

<https://doi.org/10.1038/s41586-022-04983-9>

Received: 29 March 2021

Accepted: 15 June 2022

Published online: 24 August 2022

 Check for updates

Quanquan Pang¹✉, Jiashen Meng^{1,2,3}, Saransh Gupta⁴, Xufeng Hong¹, Chun Yuen Kwok⁵, Ji Zhao³, Yingxia Jin^{3,6}, Like Xu³, Ozlem Karahan³, Ziqi Wang³, Spencer Toll³, Liqiang Mai^{2,7}, Linda F. Nazar⁵, Mahalingam Balasubramanian⁸, Badri Narayanan⁴ & Donald R. Sadoway³✉

Although batteries fitted with a metal negative electrode are attractive for their higher energy density and lower complexity, the latter making them more easily recyclable, the threat of cell shorting by dendrites has stalled deployment of the technology^{1,2}. Here we disclose a bidirectional, rapidly charging aluminium–chalcogen battery operating with a molten-salt electrolyte composed of NaCl–KCl–AlCl₃. Formulated with high levels of AlCl₃, these chloroaluminate melts contain catenated Al_nCl_{3n+1}[−] species, for example, Al₂Cl₇[−], Al₃Cl₁₀[−] and Al₄Cl₁₃[−], which with their Al–Cl–Al linkages confer facile Al³⁺ desolvation kinetics resulting in high faradaic exchange currents, to form the foundation for high-rate charging of the battery. This chemistry is distinguished from other aluminium batteries in the choice of a positive elemental-chalcogen electrode as opposed to various low-capacity compound formulations^{3–6}, and in the choice of a molten-salt electrolyte as opposed to room-temperature ionic liquids that induce high polarization^{7–12}. We show that the multi-step conversion pathway between aluminium and chalcogen allows rapid charging at up to 200°C, and the battery endures hundreds of cycles at very high charging rates without aluminium dendrite formation. Importantly for scalability, the cell-level cost of the aluminium–sulfur battery is projected to be less than one-sixth that of current lithium-ion technologies. Composed of earth-abundant elements that can be ethically sourced and operated at moderately elevated temperatures just above the boiling point of water, this chemistry has all the requisites of a low-cost, rechargeable, fire-resistant, recyclable battery.

Although batteries fitted with a metal negative electrode are attractive for their higher energy density and lower complexity (facilitating recyclability), the threat of cell shorting by dendrites has stalled deployment of the technology. Here we show two aluminium–chalcogen chemistries, aluminium–sulfur and aluminium–selenium, operating with a molten chloroaluminate electrolyte (NaCl–KCl–AlCl₃) formulated to possess high Lewis acidity, which leads to generation of catenated Al_nCl_{3n+1}[−] species. We demonstrate that these are the key to supporting ultrafast electrodeposition of aluminium (cell charging) while vitiating dendrite formation. Advantageously, the polymerization of chloroaluminates forces the melting point of the molten salt (and hence the operating temperature of the battery) to drop below the boiling point of water. Our choice of aluminium, the most earth-abundant metal, for the negative electrode addresses the anxieties around the shortages of lithium, nickel, cobalt and graphite associated with lithium-ion battery chemistry¹³. As for the choice of positive electrode, the palette of options spans a range of compounds¹⁴, but with limited success owing to high voltage polarization and low capacity even at low rates (Supplementary Table 1 and

Extended Data Fig. 1a,b). Alternatively, even though AlCl₄[−] intercalation into graphite has given indications of high-rate operation^{15,16}, the attendant consumption of electrolyte lowers the overall energy density. Accordingly, we chose elemental chalcogen for the positive electrode. Critically, the choice of electrolyte (necessarily non-aqueous) has been almost exclusively confined to room-temperature ionic liquids, for example, 1-ethyl-3-methylimidazolium chloride (EMIC) containing AlCl₃ (refs. 7–11,14,17), which are expensive and exhibit poor rate capability owing to sluggish charge-transfer kinetics and low ion diffusivity (exemplified in Extended Data Fig. 1a,b). In our work, we deviate from the conventional wisdom of favouring ambient-temperature batteries and demonstrate that at moderately elevated temperature (for example, 110 °C) both high energy density and rapid charging can be achieved with low-cost molten chloroaluminate electrolytes.

Electrolyte charge-transfer kinetics

Owing to the formation of large covalent Al_xCl_{3x+1}[−] moieties, the alkali-chloroaluminate melts (for example, NaCl–KCl–AlCl₃) exhibit

¹School of Materials Science and Engineering, Peking University, Beijing, China. ²School of Materials Science and Engineering, Wuhan University of Technology, Wuhan, China. ³Department of Materials Science & Engineering, Massachusetts Institute of Technology, Cambridge, MA, USA. ⁴Department of Mechanical Engineering, University of Louisville, Louisville, KY, USA.

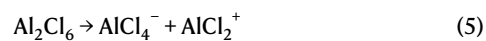
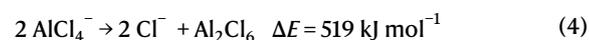
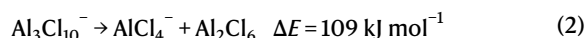
⁵Department of Chemistry, University of Waterloo, Waterloo, Ontario, Canada. ⁶School of Materials and Energy, Yunnan University, Kunming, China. ⁷State Key Laboratory of Advanced Technology for Materials Synthesis and Processing, Wuhan University of Technology, Wuhan, China. ⁸X-ray Science Division, Advanced Photon Source, Argonne National Laboratory, Argonne, IL, USA. ✉e-mail: qqpang@pku.edu.cn; dsadoway@mit.edu

a much lower eutectic point (approximately 93 °C)¹⁸ than that of simple molten-salt systems such as LiCl–NaCl–KCl (347 °C)¹⁹. This uniquely permits low-temperature operation of aluminium batteries without resorting to the use of ionic liquids for electrolytes. Although chloroaluminate melts have been used for aluminium electroplating^{20,21}, they have rarely been used in rechargeable batteries^{22,23} and never with an elemental-chalcogen positive electrode. Here a eutectic mixture of NaCl–KCl–AlCl₃ (26:13:61, mol/mol) (KCl is added to reduce the vapour pressure, which at 180 °C is quite high owing to evolution of AlCl₃) at 180 °C can support aluminium plating and stripping with low overpotential (Fig. 1a) and high coulombic efficiency (CE) (99.0–99.8% CE under galvanostatic cycling at 20 and 50 mA cm⁻²) (Extended Data Fig. 1c,d). As aluminium metal does not spontaneously react with the alkali-chloroaluminate melt, in principle the CE of an aluminium electrode can reach close to unity depending on the plating morphology. Further efforts to improve the CE beyond 99.9% (that is, increasing the compactness of the Al deposit) include using levelling agents or sacrificial film-forming additives^{24,25}, tuning the Lewis acidity of the melt and applying stack pressure^{26,27}. We demonstrate that the chalcogen electrodes (S, Se, Te), as measured in a three-electrode beaker-type cell fitted with aluminium counter and reference electrodes (Fig. 1b) exhibit stable bidirectional redox chemistry with the primary cathodic peaks at 1.05 V, 0.93 V and 0.45 V, respectively, which are consistent with values calculated from the free-energy change assuming conversion to aluminium chalcogenide, Al₂Ch₃ (1.09 V, 0.96 V, 0.57 V, where Ch denotes chalcogen).

We quantified the charge-transfer kinetics in two rather different electrolyte systems, one an ionic liquid and one a molten salt, by measuring the exchange current, *I*₀, of Al|Al symmetric cells (Fig. 1c and Extended Data Fig. 1e,f). In the ionic-liquid electrolyte, EMIC–AlCl₃ 1:1.3, which is thermally stable over the entire temperature range, the variation of *I*₀ with temperature exhibits an Arrhenius behaviour with an activation energy of 0.26 eV. Increasing the temperature from 25 °C to 110 °C and 180 °C shows a 25- and 65-fold increase in *I*₀, respectively. Impressively, compared to EMIC–AlCl₃ the NaCl–KCl–AlCl₃ melt supports an *I*₀ about one order of magnitude higher. This indicates much faster charge-transfer kinetics and hence faster Al³⁺ desolvation, which forms the foundation for the high rate capability in a battery. Incidentally, this cannot be attributed to more rapid mass transport, as the diffusivity of Al³⁺ in the EMIC–AlCl₃ is actually about three times higher than that in NaCl–AlCl₃ as calculated by ab initio molecular dynamics (AIMD) simulations in which a solvent:AlCl₃ ratio of 2:3 is used at 180 °C (KCl is omitted for clarity) (Extended Data Fig. 2c). Furthermore, the experimentally measured ionic conductivities of the two electrolytes differ only slightly from one another (Extended Data Fig. 1j). We also measured the Al exchange currents in NaCl–KCl–AlCl₃ at different AlCl₃ concentrations (Lewis acidities), and observed that *I*₀ is strongly dependent on the degree of chloroaluminate catenation (Extended Data Fig. 1g–i).

Our gas-phase quantum-chemical calculations of the anion clusters show that desolvation of Al³⁺ from the higher-order Al_xCl_{3x+1}⁻, for example, Al₃Cl₁₀⁻ and Al₄Cl₁₃⁻, is more energetically favourable than from lower-order AlCl₄⁻ and Al₂Cl₇⁻. Coincidentally, facile desolvation in the chloroaluminate melt engenders resistance to dendrite proliferation far superior to what is achievable in the analogous ionic liquids. Accordingly, a multi-step desolvation reaction scheme is proposed, assuming that for the first step the longer (and thus weaker) bridging Al–Cl bond (Fig. 1f) breaks and forms Al₂Cl₆ (equations (1)–(4) detailed in Extended Data Fig. 2g–j)²⁸. The reaction producing Al₂Cl₆ is even less endothermic than that for Al₄Cl₁₃⁻, and similarly the reaction producing Al₃Cl₁₀⁻ is even less endothermic than that for Al₂Cl₇⁻ and AlCl₄⁻ ($\Delta E = 63, 109, 138$ and 519 kJ mol⁻¹, respectively). In fact, in the AIMD trajectory of NaCl–AlCl₃ we observe such bond-cleavage reactions with Al₄Cl₁₃⁻ and Al₃Cl₁₀⁻, each generating Al₂Cl₆; this is not the

case in the AIMD trajectory of EMIC–AlCl₃ (Supplementary Videos 5 and 6). Indeed, in the ionic liquid the huge, elongated EMI⁺ cation impedes the collision of two distanced Al₂Cl₇⁻ (or AlCl₄⁻), which is necessary for equations (3) and (4) to proceed. We also argue that the closer proximity of small Na⁺ cations to the Al clusters (see *Z*(*r*) at *r* = 3–4 Å, Fig. 1e) causes a stronger coulombic attraction of the Cl⁻ and enables more facile Al–Cl scission (Extended Data Fig. 2k). Consequently, we propose the next steps to be the dissociation of Al₂Cl₆ into AlCl₄⁻ and AlCl₂⁺ (ref. 29), the latter converting to Al³⁺ through equations (5) and (6), which are uphill reactions driven by an applied electric field (Extended Data Fig. 2l)³⁰.



We conducted morphological studies on Al plating in the two electrolytes, at current densities of 10 mA cm⁻² and 50 mA cm⁻², with an areal capacity of 5 mAh cm⁻². The Al deposit in the NaCl–KCl–AlCl₃ melt reveals a landscape of compact crystals with well-defined facets and high conformity (10–15 μm size) at 10 mA cm⁻² and of connected platelets (5–8 μm wide, about 1 μm thick) at 50 mA cm⁻² (Fig. 1h,i and Extended Data Fig. 3a,c). The deposits in our electrolytes here are expected to pose no, or very little, threat of puncturing the separator and causing short-circuiting of the cell. By contrast, the Al deposit in EMIC–AlCl₃ shows a mixed morphology of discrete and curled needles (which form particles) at 10 mA cm⁻² and of highly porous crystals at 50 mA cm⁻² (Extended Data Fig. 3b,d). Therefore, at high current densities as shown here, the Al³⁺ desolvation can play a dominant role in determining the plating morphology. In addition, we determined (at least to the limits of detection of energy-dispersive X-ray spectroscopy) that our Al deposits are chlorine-free, that is, they contain no entrained electrolyte (Extended Data Fig. 3e,f).

Al–Se battery performance

The performance of selenium opposite aluminium was characterized in a simple binary NaCl–AlCl₃ electrolyte (melting point around 115 °C) using a Swagelok cell made in-house (Extended Data Fig. 4a). A crystalline selenium composite prepared by pyrolysis of a polyacrylonitrile–selenium mixture served as the positive electrode (Extended Data Fig. 4b–f). For clarity, we use *C*/*n* to denote a charging rate that accumulates full charge in *n* hours and *D*/*n* for a discharging rate that depletes full charge in *n* hours. As shown in Fig. 2a, the discharge reaction between electrodes of selenium and aluminium in molten NaCl–AlCl₃ at 180 °C proceeds along a rather flat voltage–time trace (averaging approximately 0.88 V) with a capacity of 655 mAh g⁻¹ at *D*/5. The cell shows a decent cycling stability, sustaining 300 mAh g⁻¹ and no voltage decay over 50 cycles at rates of *D*/5 and *C*/2 (Extended Data Fig. 5c,d). We also observe a similar stability for a cell fitted with a milled commercial selenium positive electrode (Extended Data Fig. 5e).

We evaluated the rate capability of Al–Se cells by varying the charging rates (from *C*/2 to 200C) while discharging at a fixed *D*/10 rate,

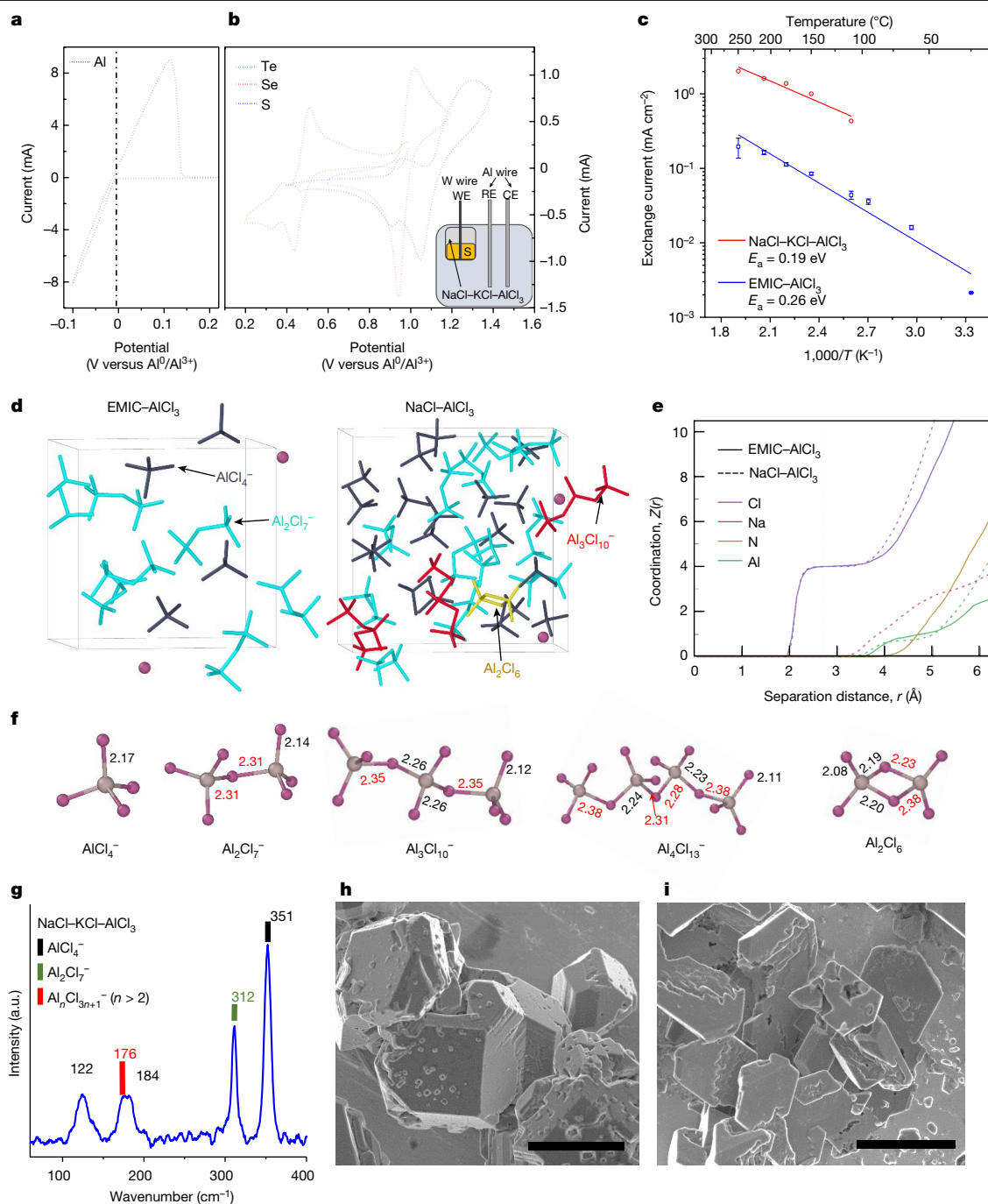


Fig. 1 | Fundamentals of the molten-salt electrolyte and aluminium-chalcogen electrochemistry. **a, b**, CV plots of aluminium metal (**a**) and chalcogen elements (**b**) as the working electrode (WE) in the cell schematically shown in the inset of **b**. CE, counter electrode; RE, reference electrode. **c**, Temperature dependence of exchange current of Al|Al symmetric cells in the two electrolytes. The error bars are standard deviations based on three measurements. **d**, Typical snapshots from the AIMD trajectories showing the different chloroaluminate solvation clusters for the two electrolytes; Cl^- , AlCl_4^- , Al_2Cl_6 , Al_2Cl_7^- and $\text{Al}_3\text{Cl}_{10}^-$ clusters are shown in purple, dark blue, gold, cyan and red, respectively. For clarity, the cations EMIC^+ and Na^+ are not displayed. The cubic boxes represent the supercells for the calculations (the

scale of the NaCl-AlCl_3 supercell is approximately 23% larger than that of EMIC-AlCl_3). **e**, The atomic coordination around Al^{3+} , $Z(r)$, as a function of bonding distance, r , by integrating the radial distribution functions obtained from AIMD simulations. **f**, The representative configuration of the clusters taken from the calculated equilibrium states; the Al and Cl atoms are shown in grey and purple, respectively, and the numbers represent the Al-Cl bond length in ångströms, with red values indicating a relatively longer distance. **g**, The Raman spectrum of the NaCl-KCl-AlCl_3 electrolyte measured at 180 °C. a.u., arbitrary units. **h, i**, The SEM images of Al plated on a Ta substrate in the molten NaCl-KCl-AlCl_3 electrolytes at 180 °C at a current density of 10 mA cm^{-2} (**h**) and 50 mA cm^{-2} (**i**) for an areal capacity of 5 mAh cm^{-2} ; scale bars, 5 μm .

mimicking practical requirements (Fig. 2b and Extended Data Fig. 5f). The selenium shows a reversible capacity of 520 mAh g^{-1} at a charging rate of $C/2$ and maintains a capacity of 190 mAh g^{-1} at 10C. When the charging rate is increased to 200C, the cell still retains a capacity of

75 mAh g^{-1} . Notably, this is not an ion-adsorption capacitive behaviour, because both charge and discharge show well-defined plateau-like voltage-time traces and differential-capacity curves (Extended Data Fig. 5g,h). Only a marginal fraction of the capacity in the applied-voltage

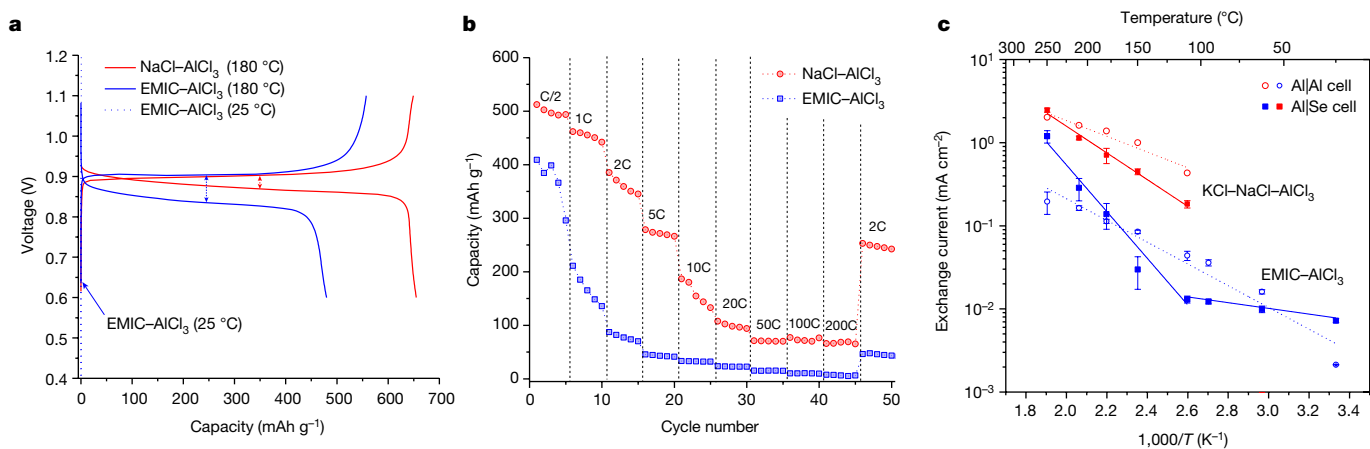


Fig. 2 | Electrochemical characterization of the Al–Se batteries. **a**, Typical voltage–capacity traces of Al–Se cells using molten-salt and ionic-liquid chloroaluminate electrolytes. **b**, Charging rate performance of Al–Se cells as a function of charging rate at a constant discharge rate ($D/10$) at 180 °C.

window comes from the carbon (Extended Data Fig. 4f). The faradaic behaviour at high rates is also confirmed by spectroscopic studies as discussed below. By contrast, the EMIC–AlCl₃ cell shows a capacity close to zero at charging rates exceeding 10C (Fig. 2b and Extended Data Fig. 5h).

To discover whether the reaction on the positive or negative electrode limits rate capability, we measured the exchange current of Al|Se cells and compared the value to that of Al|Al symmetric cells (Extended Data Fig. 1k,l). The I_0 of the Al|EMIC–AlCl₃|Se cell does not follow a monotonic Arrhenius trend; instead, a significant increase in I_0 occurs only above 150 °C (Fig. 2c), indicating a transition in the selenium reaction pathway at this temperature. Comparing the I_0 values of the Al|Se cells to those of the Al|Al cells, we find that the selenium reaction on the positive electrode is always rate determining for the NaCl–KCl–AlCl₃ cell, whereas the EMIC–AlCl₃ cell is rate limited by the aluminium electrode reaction above 150 °C. In any event, the performance of Al|molten chloroaluminate|Se cells is demonstrably far superior to that of Al|ionic liquid|Se cells.

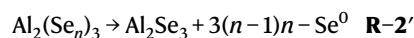
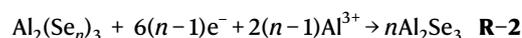
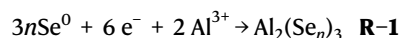
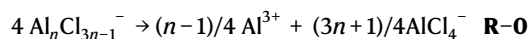
Redox mechanisms

As reported in the literature, ultrafast cycling (approximately 100C) has been shown only in intercalation electrodes, such as Nb₆W₅O₅₅ (Li⁺)³¹, graphite (AlCl₄[−])³² and phenanthrenequinone (AlCl₂⁺)³³. Our demonstration of conversion-type electrodes that exploit a reaction involving lattice reconstruction expands the palette of conventionally regarded high-rate materials. To explain such observations we therefore interrogated the selenium reaction mechanism by operando X-ray absorption fine-structure spectroscopy (XAFS), combined with operando X-ray diffraction (XRD) (detailed in the Methods). The operando mode is necessary to allow us to capture the dynamics of species formation at the elevated operating temperature (180 °C).

Extended Data Figs. 6 and 7 present details of the components that comprise the Se K-edge X-ray absorption spectra and extended X-ray absorption fine structure (EXAFS) fitting. Linear combination fitting of the XAFS spectra using the three identified compositions as standards clearly reveals two reaction regions (Fig. 3e and Extended Data Fig. 8a). In region I, Se⁰ is consumed with the formation of Al₂(Se_{*n*})₃ (reaction **R-1**); Al₂Se₃ starts to form at a state of discharge (SOD) of 30%, owing to the further reduction of Al₂(Se_{*n*})₃ (reaction **R-2**). In region II, the Al₂(Se_{*n*})₃ is consumed with the rapid formation of Al₂Se₃ (**R-2**), and the Se⁰ fraction remains relatively constant. Nevertheless,

c, Comparison of the temperature dependence of the exchange current of Al|Se cells (solid dots) and Al|Al cells (open dots); the data fit is log-linear indicating an Arrhenius behaviour. The error bars are derived from the standard deviation based on three measurements.

a separate operando XRD experiment that specifically monitors crystalline selenium (*c*-Se⁰) shows a continuous decrease of *c*-Se⁰ until the end of the discharge (Fig. 3f and Extended Data Fig. 8b), which implies that non-crystalline Se⁰ (*n*-Se) is formed in region II, probably by a disproportionation reaction (reaction **R-2'**) concurrently with **R-1** and **R-2** (ref. ³⁴). Towards the end of the discharge, the reaction **R-2'** ceases, whereas the Se⁰ and Al₂(Se_{*n*})₃ are fully consumed via **R-1** and **R-2**. The proposed reaction scheme is aligned with the cell impedance data measured in situ, where the charge-transfer resistance varies with the state of charge (Extended Data Fig. 8fc,d). Importantly, rather than a single-step conversion between Se⁰ and Al₂Se₃, the reaction of selenium in the molten chloroaluminate is mediated by the formation of Al₂(Se_{*n*})₃, which shows low but essential solubility as indicated by the colour of such a solution (Extended Data Fig. 8e). The reaction front is thus unhindered by the formation of solid products, thereby supporting the ultrafast charge-transfer kinetics. Furthermore, as confirmed by XRD, the discharged products (Al₂Se₃) are non-crystalline. Consequently, their formation avoids the nucleation-energy penalty incurred by the analogous reaction at the positive electrode in ambient-temperature Li–Se_{*x*} batteries³⁵. Importantly, the XAFS spectra of selenium electrodes charged at high rates (representatively at 20C and 50C) show the presence of elemental Se⁰ and a fraction of Al₂(Se_{*n*})₃, which effectively proves a faradaic behaviour for the selenium at high charging rates (Extended Data Fig. 8f–h).



High-capacity, fast-charging Al–S battery

For lower-cost, higher-capacity and lower-temperature operation, we also describe an Al–S battery that operates at 110 °C owing to an electrolyte consisting of NaCl–KCl–AlCl₃, which has a eutectic at approximately 93 °C (ref. ¹⁸) and lower volatility than the KCl-free

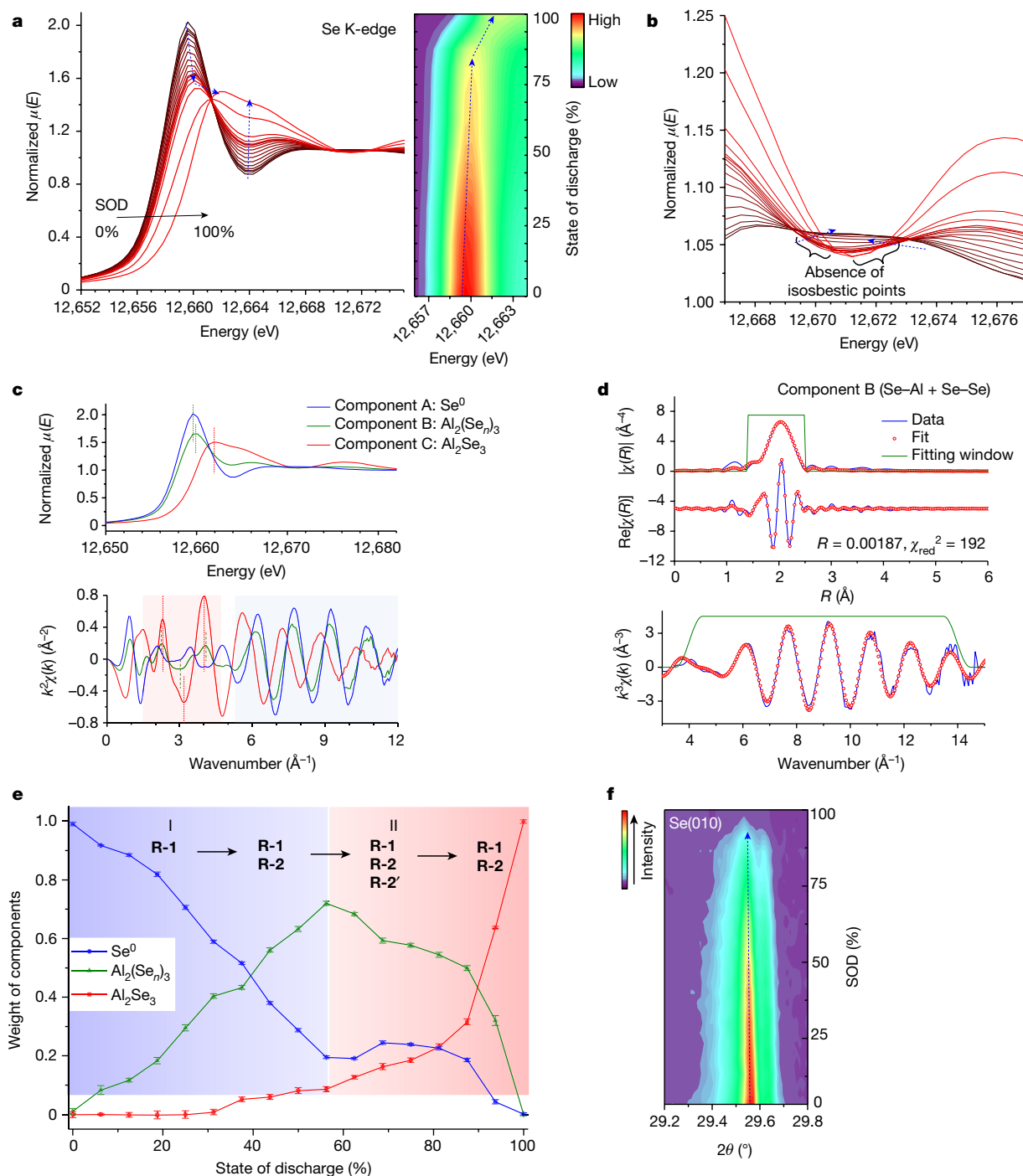


Fig. 3 | X-ray studies revealing the reaction pathway of the Al/NaCl-AlCl₃/Se battery on discharge at $T = 180$ °C. **a**, Se K-edge XANES spectra (plotted as absorbance normalized on absorbing atom basis ($\mu(E)$, linear absorption coefficient) versus E , incident photon energy) of the selenium positive electrode obtained operando during the discharge of the Al-Se battery, as shown stacked (left) and in the contour map (right). **b**, The magnified XANES spectra in a representative region that shows the isosbestic points shared by the first few but not all of the spectra. **c**, XANES spectra and the k -space EXAFS $k^2\chi(k)$ oscillations of the three identified primary components (the dashed line indicates the shift of the 'cross points'). **d**, The best-fit modes of the EXAFS data

of component B by including two paths: Se-Al and Se-Se (top, R space; bottom, k space, where R represents a pair correlation distance (such as Se-Al or Se-Se) for those contributions that involve two-body correlations, χ is extracted from the raw XAFS function (X-ray absorption fine-structure spectrum) and k is the photoelectron wavenumber). **e**, The weight of each component as a function of the SOD as quantified by linear combination fitting; the proposed reactions in each of the regions are noted. **f**, The contour map showing the evolution of the Se(010) XRD peak collected operando as a function of SOD. The blue dotted arrows in **a**, **b** and **f** indicate the variation as the SOD increases from 0 to 100%.

melt at a comparable AlCl₃ concentration. Extra care has to be taken to avoid water contamination in the acidic melt to prevent formation of H₂S in the sulfur chemistry. We demonstrate the electrochemistry using a sulfur-graphene composite in which the graphene

contributes marginal capacity (Extended Data Fig. 9a-c). Sulfur shows a flat voltage-time trace averaging 1.05 V and initial capacity reaching 1,350 mAh g⁻¹ at D/5 (theoretical: 1,675 mAh g⁻¹, Fig. 4a). The polarization is as low as 50 mV, which is in sharp contrast to that

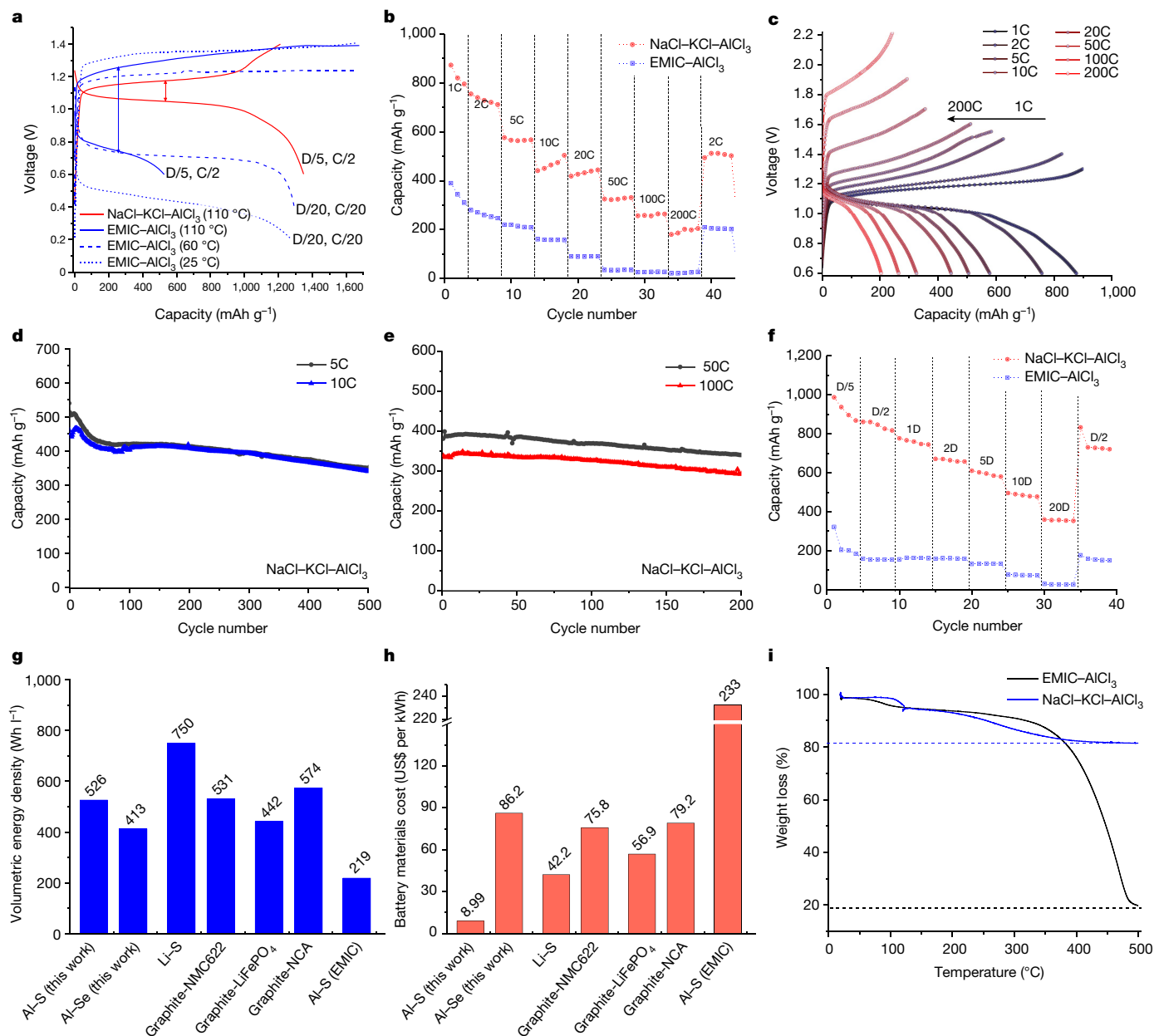


Fig. 4 | Electrochemical characterization and practical projection of the Al|NaCl-KCl-AlCl₃S battery. **a**, Typical voltage–capacity traces of Al|NaCl-KCl-AlCl₃S cells at different temperatures. **b, c**, The charge rate performance (**b**) and the voltage–capacity traces (**c**) of Al|NaCl-KCl-AlCl₃S cells at different charging rates and constant discharging rate (D/2) at 110 °C. **d, e**, Cycling stability (discharge capacity at a rate of D/2) of Al|NaCl-KCl-AlCl₃S cells at charging rates of 5–10C (**d**) and 50–100C (**e**) after conditioning cycles following protocols described in the Methods. **f**, Discharge rate performance of Al|NaCl-KCl-AlCl₃S cells at varying discharging rates and constant charging rate (0.5C)

measured in EMIC–AlCl₃; 450 mV at 25 °C (D/20), 250 mV at 60 °C (D/20) and 205 mV at 110 °C (D/5). Furthermore, the Al|EMIC–AlCl₃S cell experiences extensive overcharge and very low sulfur utilization at all temperatures (for example, 525 mA h^{–1} at 110 °C, Fig. 4a), indicating that there is significant dissolution of intermediate species in the electrolyte.

With a constant discharge rate of D/2, the Al–S cell exhibits a high capacity of 500 mA h^{–1} at a charging rate of 10C, which slightly decreases to 430 and 360 mA h^{–1} at 20C and 50C, respectively (Fig. 4b,c). Even at extreme charging rates of 100C and 200C

at 110 °C. **g, h**, The cell-level energy density (**g**) and cost (**h**) of the aluminium–chalcogen batteries in comparison to those of contemporary battery systems, calculated based on a pouch cell configuration including the electrode laminate, current collectors, tabs, packaging and so on (as detailed in Extended Data Table 1). **i**, The volatility test of the two electrolytes as measured by thermogravimetric analysis (TGA) under argon atmosphere, showing the much lower volatility of molten NaCl–KCl–AlCl₃ as compared to that of the EMIC–AlCl₃ ionic liquid at comparable AlCl₃ concentrations. The dashed lines indicate the asymptotic limits of AlCl₃ volatility.

(335 A g^{–1} and 670 mA cm^{–2}), the cell still shows high capacity of 280 and 210 mA h^{–1}, respectively. At all charging rates, the cell shows well-defined, non-capacitive voltage–time traces (Fig. 4c and Extended Data Fig. 9d). By contrast, the cell fitted with EMIC–AlCl₃ shows close to zero capacity at 50C and higher temperatures (Extended Data Fig. 9e). The ultrafast charging capability in NaCl–KCl–AlCl₃ is not unique to a particular carbon host material (Extended Data Fig. 9f,g). After a number of conditioning cycles following protocols stated in the Methods, the cells can sustain hundreds of cycles at high charging rates of 5–10C and ultrahigh rates of 50–100C (Fig. 4d,e).

The Al–S chemistry also shows a good fast-discharging capability in NaCl–KCl–AlCl₃: 670 and 360 mAh g⁻¹, respectively, at 2D and 20D, which is much improved compared to that in EMIC–AlCl₃ (Fig. 4f and Extended Data Fig. 9h,i).

The discrepancy between the demonstrated charging and discharging rate capabilities is due to asymmetry in the Al³⁺ solvation and desolvation processes, such as the asymmetry attributed to the molecular structure of the AlCl₃-rich chloroaluminate melt, which is very acidic in the Lewis sense; hence, it is kinetically more favourable to exsolve AlCl₃ than to dissolve it^{36,37}. When the cell is discharging, the less favoured Al³⁺ solvation (accompanied by AlCl₃ dissolution) occurs at the planar Al negative electrode, which carries a much higher local current density than does the powdered sulfur electrode with its higher surface area. This means that on discharge the reaction at the negative electrode is rate limiting. On charge, it is the kinetics of Al³⁺ deposition that is favoured; hence, in spite of the difference in electrode surface areas, a higher rate capability is more easily attainable on charge than on discharge. Importantly, in the Al–S cell even after cycling at high charging rates we see no evidence of Al dendrite growth that could lead to shorting of the cell (Extended Data Fig. 9j,k). We speculate that dendrite growth is impeded by the combination of the presence of large higher-order catenated chloroaluminate moieties (Al₂Cl₇⁻, Al₃Cl₁₀⁻, and so on), which sets a high threshold current for dendrite proliferation, along with the presence of trace amounts of dissolved sulfide, which has been reported to act as a levelling agent³⁸.

Outlook

Our electrochemical data show that the projected cell-level energy density of the Al|NaCl–KCl–AlCl₃|S battery can achieve 526 Wh l⁻¹, which is on a par with that of graphite–NMC622 (LiNi_{0.6}Mn_{0.2}Co_{0.2}O₂) and other lithium-ion batteries (Fig. 4g; including the electrode laminate, current collectors, tabs, packaging, as detailed in Extended Data Table 1). On a practical note, we demonstrate that sulfur electrodes with a high loading of 12.0 mg cm⁻² can sustain a high capacity of 520 mAh g⁻¹ over 100 cycles at C/5 (Extended Data Fig. 10a). We attribute full accessibility of electrode capacity to the advantageously low surface tension of the chloroaluminate melt³⁹. Furthermore, to avoid electrolyte diffusion limitation from the lack of percolation and to demonstrate the fast-charging capability of thick electrodes, we prepared a three-dimensional interconnected reduced graphene oxide–sulfur composite electrode—endowed with long-range and short-range electrolyte penetration by the rich macro- and meso-pores, respectively—that shows great fast-charging capability at an areal sulfur loading of 7.1 mg cm⁻² (Extended Data Fig. 10b–e). Inspired by the liquid metal battery⁴⁰, we see the potential of the new chemistry when operating in a modified ‘tri-layer’ cell configuration: Al_(solid)|NaCl–KCl–AlCl₃(liquid)|S_(liquid) (top to bottom, Extended Data Fig. 10f).

Importantly, our battery has a two-fold economic promise. First, given the high earth abundance of all components, aluminium, sulfur, NaCl, KCl and AlCl₃, the estimated cell-level cost of our Al–S battery is as low as US\$8.99 per kWh, which is 12–16% of that of today’s lithium-ion batteries (Fig. 4h; see details in Extended Data Table 1). We also show that the use of low-grade aluminium (for example, food-packaging foil) in the negative electrode does not result in appreciable deterioration in cell performance (Extended Data Fig. 10k). This allows us to take advantage of commercial-grade metal as produced by today’s aluminium industry. Second, with such a mild superambient operating temperature potentially as low as 90 °C, the battery will not require an active cooling system, which is absolutely critical for lithium-ion batteries in large format; instead, the moderately elevated temperature can be maintained by the combination of internal joule heating generated while cycling and by proper thermal insulation. Of utter importance and distinctly advantageous, the molten-salt electrolyte is thermally stable and

non-volatile over the range of operating temperature and beyond 500 °C (Fig. 4i). It has not escaped our notice that its immunity to thermal runaway and fire⁴¹ (Fig. 4i) makes this battery chemistry especially attractive for electric vehicles. Finally, adaptation of the aluminium/molten chloroaluminate/chalcogen paradigm to other metals may unlock other multivalent battery chemistries that up to now remain stalled owing to sluggish ion transport in the electrolyte and to poor desolvation kinetics at the negative electrode resulting in dendrite formation and cell shorting.

Online content

Any methods, additional references, Nature Research reporting summaries, source data, extended data, supplementary information, acknowledgements, peer review information; details of author contributions and competing interests; and statements of data and code availability are available at <https://doi.org/10.1038/s41586-022-04983-9>.

- Chen, S., Dai, F. & Cai, M. Opportunities and challenges of high-energy lithium metal batteries for electric vehicle applications. *ACS Energy Lett.* **5**, 3140–3151 (2020).
- Varzi, A. et al. Current status and future perspectives of lithium metal batteries. *J. Power Sources* **480**, 228803 (2020).
- Muldoon, J., Bucur, C. B. & Gregory, T. Quest for nonaqueous multivalent secondary batteries: magnesium and beyond. *Chem. Rev.* **114**, 11683–11720 (2014).
- Jayaprakash, N., Das, S. K. & Archer, L. A. The rechargeable aluminum-ion battery. *Chem. Commun.* **47**, 12610–12612 (2011).
- Geng, L., Lv, G., Xing, X. & Guo, J. Reversible electrochemical intercalation of aluminum in Mo₆S₈. *Chem. Mater.* **27**, 4926–4929 (2015).
- Kotetsu, T. et al. Reversible magnesium and aluminium ions insertion in cation-deficient anatase TiO₂. *Nat. Mater.* **16**, 1142–1148 (2017).
- Xia, S., Zhang, X.-M., Huang, K., Chen, Y.-L. & Wu, Y.-T. Ionic liquid electrolytes for aluminum secondary battery: influence of organic solvents. *J. Electroanal. Chem.* **757**, 167–175 (2015).
- Gao, T. et al. A rechargeable Al/S battery with an ionic-liquid electrolyte. *Angew. Chem. Int. Ed.* **55**, 9898–9901 (2016).
- Cohn, G., Ma, L. & Archer, L. A. A novel non-aqueous aluminum sulfur battery. *J. Power Sources* **283**, 416–422 (2015).
- Yu, X. & Manthiram, A. Electrochemical energy storage with a reversible nonaqueous room-temperature aluminum-sulfur chemistry. *Adv. Energy Mater.* **7**, 1700561 (2017).
- Yu, X., Boyer, M. J., Hwang, G. S. & Manthiram, A. Room-temperature aluminum-sulfur batteries with a lithium-ion-mediated ionic liquid electrolyte. *Chem* **4**, 586–598 (2018).
- Reed, L. D., Ortiz, S. N., Xiong, M. & Menke, E. J. A rechargeable aluminium-ion battery utilizing a copper hexacyanoferrate cathode in an organic electrolyte. *Chem. Commun.* **51**, 14397–14400 (2016).
- Turcheniuk, K., Bondarev, D., Singhal, V. & Yushin, G. Ten years left to redesign lithium-ion batteries. *Nature* **559**, 467–470 (2018).
- Schoetz, T., Ponce de Leon, C., Ueda, M. & Bund, A. State of the art of rechargeable aluminum batteries in non-aqueous systems. *J. Electrochem. Soc.* **164**, A3499–A3502 (2017).
- Song, Y. et al. A long-life rechargeable Al ion battery based on molten salts. *J. Mater. Chem. A* **5**, 1282–1291 (2017).
- Chen, H. et al. Ultrafast all-climate aluminum-graphene battery with quarter-million cycle life. *Sci. Adv.* **3**, eaao7233 (2017).
- Zhang, Y., Liu, S., Ji, Y., Ma, J. & Yu, H. Emerging nonaqueous aluminum-ion batteries: challenges, status, and perspectives. *Adv. Mater.* **30**, 1706310 (2018).
- Midorikawa, R. Electrolytic refining of aluminum. II. The melting point of the system AlCl₃–NaCl–KCl. *Denki Kagaku* **23**, 127–129 (1955).
- Lu, G., Lai, T., He, M. & Liu, X. Experimental measurement and thermodynamic optimization of the phase diagram of LiCl–NaCl–KCl system. *Chin. Sci. Bull.* **65**, 641–648 (2019).
- Stafford, G. R. The electrodeposition of an aluminum-manganese metallic glass from molten salts. *J. Electrochem. Soc.* **136**, 635–639 (1989).
- Howie, R. C. & Macmillan, D. W. The electrodeposition of aluminium from molten aluminium chloride/sodium chloride. *J. Appl. Electrochem.* **2**, 217–222 (1972).
- Koura, N. A preliminary investigation for an Al/AlCl₃–NaCl/FeS₂ secondary cell. *J. Electrochem. Soc.* **127**, 1529–1531 (1980).
- Berrettoni, M., Tossici, R., Zamponi, S., Marassi, R. & Mamantov, G. A cyclic voltammetric study of the electrochemical behavior of NiS₂ in molten NaCl saturated NaAlCl₄ melts. *J. Electrochem. Soc.* **140**, 969–973 (1993).
- Fellner, P., Chrenková-Paučířová, M. & Matiašovský, K. Electrolytic aluminium plating in molten salt mixtures based on AlCl₃: I: influence of the addition of tetramethylammonium chloride. *Surface Tech.* **14**, 101–108 (1981).
- Li, Q., Hjuler, H. A., Berg, R. W. & Bjerrum, N. J. Electrochemical deposition and dissolution of aluminum in NaAlCl₄ melts: influence of MnCl₂ and sulfide addition. *J. Electrochem. Soc.* **137**, 2794 (1990).
- Weber, et al. Long cycle life and dendrite-free lithium morphology in anode-free lithium pouch cells enabled by a dual-salt liquid electrolyte. *Nat. Energy* **4**, 683 (2019).
- Louli, J. et al. Diagnosing and correcting anode-free cell failure via electrolyte and morphological analysis. *Nat. Energy* **5**, 693 (2020).
- Yang, H. et al. An aluminum-sulfur battery with a fast kinetic response. *Angew. Chem. Int. Ed.* **57**, 1989–1902 (2018).

29. Akdeniz, Z., Pastore, G. & Tosi, M. P. An ionic model for molecular units in molten aluminium trichloride and alkali chloroaluminates. *Phys. Chem. Liq.* **32**, 191–209 (1996).
30. Boxall, L. G., Jones, H. L. & Osteryoung, R. A. Solvent equilibria of AlCl_3 -NaCl melts. *J. Electrochem. Soc.* **120**, 223–231 (1973).
31. Griffith, K. J., Wiaderek, K. M., Cibir, G., Marbelle, L. E. & Grey, C. P. Niobium tungsten oxides for high-rate lithium-ion energy storage. *Nature* **591**, 556–563 (2018).
32. Lin, M.-C. et al. An ultrafast rechargeable aluminium-ion battery. *Nature* **520**, 325–328 (2015).
33. Kim, D. J. et al. Rechargeable aluminium organic batteries. *Nat. Energy* **4**, 51–59 (2019).
34. Cuisinier, M. et al. Sulfur speciation in Li-S batteries determined by operando X-ray absorption spectroscopy. *J. Phys. Chem. Lett.* **4**, 3227–3232 (2013).
35. Cui, Y. et al. (De)Lithiation mechanism of Li/SeS_x (x = 0–7) batteries determined by in situ synchrotron X-ray diffraction and x-ray absorption spectroscopy. *J. Am. Chem. Soc.* **135**, 8047–8056 (2013).
36. Wang, C. & Hussey, C. L. Aluminum anodization in the low-melting LiAlBr_2 - NaAlCl_4 - KAlCl_4 molten salt. *ECS Trans.* **64**, 257–265 (2014).
37. Stafford, G. R. & Haarberg, G. M. The electrodeposition of Al-Nb alloys from chloroaluminate electrolytes. *Plasmas Ions* **1**, 35–44 (1999).
38. Li, Q., Hjuler, H. A., Berg, R. W. & Bjerrum, N. J. Electrochemical deposition and dissolution of aluminum in NaAlCl_4 melts. Influence of MnCl_2 and sulfide addition. *J. Electrochem. Soc.* **137**, 2794–2798 (1990).
39. Sato, Y., Fukasawa, M., Abe, K. & Yamamura, T. Surface tensions of basic NaCl- AlCl_3 and LiCl- AlCl_3 binary melts. *Electrochemistry (Tokyo)* **67**, 563–567 (1999).
40. Wang, K. et al. Lithium-antimony-lead liquid metal battery for grid-level energy storage. *Nature* **514**, 348–350 (2014).
41. Tripathy, P. K. et al. Aluminum electroplating on steel from a fused bromide electrolyte. *Surf. Coat. Tech.* **258**, 652–663 (2018).

Publisher's note Springer Nature remains neutral with regard to jurisdictional claims in published maps and institutional affiliations.

© The Author(s), under exclusive licence to Springer Nature Limited 2022

Methods

Preparation of the electrolytes

The preparation of inorganic chloroaluminates, NaCl–AlCl₃ and NaCl–KCl–AlCl₃ follows the eutectic ratio as documented in phase diagrams^{42,43}. NaCl (99.99%, Sigma-Aldrich) and KCl (99.95%, Alfa Aesar) were dried in a muffle furnace for 72 h before use. AlCl₃ (99.99%, Alfa Aesar) was used as received. The precursor powders were mixed in a specific molar ratio, NaCl:AlCl₃ (37:63) or NaCl:KCl:AlCl₃ (26:13:61), and heat soaked in a closed weighing bottle at 180 °C for 24 h. The melt was cooled to room temperature, crushed and ground into powder for battery assembly. NaCl–KCl–AlCl₃ electrolytes of other compositions (29:14:57, 34:17:49) were also prepared for the exchange current study. The EMIC–AlCl₃ ionic-liquid electrolyte at the optimal molar ratio of 1:1.3 as described in the literature was prepared by slowly adding AlCl₃ powder into EMIC (>98%, TCI America) under rigorous stirring. The EMIC was baked in vacuo at 120 °C overnight before use. All the preparations were performed inside the glovebox (O₂ <0.1 ppm, H₂O <0.1 ppm). Water in the chloroaluminate electrolyte can react with AlCl₃ to form HCl, which then reacts with sulfides to form H₂S.

Preparation of selenium electrodes

In cells used for cycle testing (charge/discharge) and rate performance (Fig. 2 and Extended Data Fig. 5), the selenium–carbon composite for the positive electrode was synthesized by pyrolysis of the mixture of polyacrylonitrile and selenium. The polyacrylonitrile (average molecular weight $M_w = 150,000$) powder was first mixed with selenium (99.999%, Alfa Aesar) at a 1:3 weight ratio by ball milling for 10 min. The mixture was then pelletized and loaded in a dry fused quartz tube, which was then evacuated and sealed for heat treatment at 600 °C for 3 h (ramp rate = 3 °C min⁻¹, furnace cooling). The reactions on heating included dehydrogenation and cyclization of the polymer chain along with chemically bonded selenium, followed by carbonization of the matrix⁴⁴. The selenium in the composite exists as a crystalline phase (Extended Data Fig. 4d) and is homogeneously embedded in the carbon matrix. The same carbon material (selenium-free) was prepared by pyrolysis of solely polyacrylonitrile using the same heating procedure to reveal the capacity contribution from the carbon itself. Also, a simple selenium composite was also prepared by ball-milling selenium with Super P carbon (MTI Corp.) in a 70:30 weight ratio for 10 min (the selenium weight fraction is 70%). This selenium composite was also used for galvanostatic intermittent titration (GITT) and operando XRD studies. For the EXAFS experiment, to obtain good homogeneity and smaller selenium particle size, the selenium composite was prepared by a thermal diffusion method, where the Super P/selenium milled mixture (70:30, wt/wt) was heat soaked at 300 °C for 12 h in the glovebox. To prepare the selenium electrodes, the respective selenium–carbon composite was mixed with Super P carbon, polytetrafluoroethylene (Sigma-Aldrich) at an 8:1:1 weight ratio by hand grinding. The slurry was made by stirring the mixture in 2-propanol (HPLC grade, Sigma-Aldrich). The electrodes were made by drop casting the slurry on P50 carbon papers (Fuel Cell Store) (diameter 10 mm) and dried at 90 °C in vacuo for 6 h. The areal loading of selenium is 3.2–3.5 mg cm⁻².

Preparation of sulfur electrodes

The proof-of-concept sulfur composite was prepared by the thermal diffusion approach. The sulfur (Alfa Aesar) and graphene (ACS Materials) were mixed (50:50, wt/wt) by grinding and then heat soaked at 155 °C for 12 h to obtain the sulfur composite. The sulfur electrodes were prepared in the same way as the selenium electrode (sulfur:Super P:polytetrafluoroethylene = 8:1:1 in 2-propanol), except that the electrodes were dried at 60 °C in vacuo for 6 h. The areal loading of sulfur in a typical electrode is 1.5–2.0 mg cm⁻². Sulfur-free graphene electrodes were made in the same way to reveal the contribution of graphene to the total capacity. High-loading electrodes (12.0 mg cm⁻²) were also prepared

in the same way except that the electrodes were cold pressed under a 1 ton force before use. A Ketjen Black sulfur electrode was also made by using a Ketjen Black/S composite (prepared by thermal diffusion with 60 wt% of sulfur) with a sulfur loading of 2.0 mg cm⁻².

Electrochemical measurements

The cyclic voltammetry (CV) measurements were performed in a three-electrode beaker-type cell at 180 °C as schematically shown in Fig. 1a. A tungsten crucible with an inner diameter of 20 mm contained the molten-salt electrolyte (NaCl–KCl–AlCl₃). Two aluminium wires (99.99%, diameter 1 mm, Alfa Aesar) were immersed in the electrolyte, one serving as the counter electrode and one serving as the reference electrode. For the aluminium plating study, a tungsten wire (99.9%, diameter 1 mm, Alfa Aesar) served as the working electrode. For the sulfur study, molten sulfur contained in a separate fused quartz crucible, which was submerged in the electrolyte, served as the working electrode. For the studies of selenium and tellurium plating, the working electrodes were prepared by dipping the tungsten wire in a melt of selenium or tellurium, respectively. Solidified chalcogen metal coating the tungsten served as the active electrode. The functional surface areas of the three electrodes were thus approximately equal and similar to the geometric area of the tungsten wire. The CV was performed with a Solartron EM potentiostat at a scanning rate of 10 mV s⁻¹.

The galvanostatic cycle testing was performed using in-house-designed Swagelok cells as schematically shown in Extended Data Fig. 3a. To prevent the corrosion of the stainless steel cell body by the chloroaluminate melts, a protective sheath was placed in the cell to contain the electrodes and electrolyte. Glass fibre membrane (GF-D, Whatman) was used as the separator and aluminium foil (99.99%, 100 μm thick, Alfa Aesar, diameter 11 mm) was used as the negative electrode. A stainless steel compression spring and a molybdenum foil spacer maintained the pressure. A molybdenum rod served as the external current collector for both electrodes. For the Al metal plating/stripping measurement, a Ta foil served as the working electrode and the Al foil served as the counter electrode. Galvanostatic cycling (Al plating/stripping) was performed at current density of 20 mA cm⁻² and 50 mA cm⁻² with 1 mAh cm⁻² capacity (charging voltage cut at 1.0 V). An amount of 80 mg of NaCl–AlCl₃ or 90 mg of NaCl–KCl–AlCl₃ (about 50 μl) served as the electrolyte in the Al–Se and Al–S cells, respectively. About 80 μl of the EMIC–AlCl₃ solution served as the electrolyte in the ionic-liquid cells. The cycling experiments were performed using an Arbin 2000T cyler. For clarity in describing the cycling rates that differ between charging and discharging, we use the notation 1D (and 1C) to denote a discharge (and charge) rate, which corresponds to full discharge (and charge) in one hour. The voltage–time traces shown in Fig. 2a and Fig. 4a are the initial cycle of the corresponding cells; the rate performances shown in Fig. 2b and Fig. 4b are after the initial conditioning cycle, which was performed at D/10 and C/5 rates for selenium and D/2 and C/2 rates for sulfur. The rate measurements of Al–Se cells were conducted at a constant discharge rate of D/10 and a plurality of charge rates up to 200C (1C or 1D = 678 mAh g⁻¹ for selenium) and the same protocol was used for sulfur except that the discharge rate was D/2 (1C or 1D = 1,675 mAh g⁻¹ for sulfur). The discharge rate measurement for sulfur was performed at a constant charge rate of 1C and a plurality of discharge rates up to 20D. The areal current densities for a 3.2 mg cm⁻² loaded selenium cathode are 1.085, 2.17, 4.34, 10.85, 21.7, 43.4, 108.5, 217 and 434 mA cm⁻² for the rates of C/2, 1C, 2C, 5C, 10C, 20C, 50C, 100C and 200C, respectively. The areal current densities for a 1.5 mg cm⁻² loaded sulfur cathode are 2.52, 5.04, 12.6, 25.2, 50.4, 126, 252 and 504 mA cm⁻² for the rates of 1C, 2C, 5C, 10C, 20C, 50C, 100C and 200C respectively. The cycling stability measurements shown in Fig. 4d,e were after a number of conditioning cycles that serve to achieve stabilized capacity. Specifically, the conditioning cycles were carried out by stepwise increasing the charge rates from 1C to the targeted rates, with three cycles at each step. We did observe that the conditioning cycles using

such a protocol are necessary to achieve stabilized capacity at high rates for Al–S chemistry. The GITT measurements were performed on Al–Se cells with milled bulk selenium electrodes using the following protocol: a 20 min discharge current pulse of $C/10$ followed by a 60 min rest.

The cell-level energy density and cost of the aluminium–chalcogen batteries in comparison to that of lithium-ion batteries were calculated based on a virtual cell configuration with realistic parameters as tabulated in Extended Data Table 1 using the Battery Forward Designer software. The compacted density and porosity of the electrode, the amount of electrolyte and the size of the current collector, tab and package were determined using empirical parameters from the literature or the industry, assuming a 065070 pouch cell geometry. The specific capacity and voltage values were based on literature values. The energy density was calculated by dividing the total energy by the total volume of the pouch cell. The price was the latest market price or the projected price if market price was unavailable and therefore may be subject to fluctuation errors.

Exchange current and electrolyte conductivity measurements

The exchange currents of Al|Al and Al|Se cells were determined by linear sweep voltammetry (LSV) using the in-house-designed Swagelok cells as described above. The Al|Al symmetric cells (aluminium foil as both electrodes) and Al|Se full cells (Se/carbon as the positive electrode and Al foil as the negative electrode) were assembled using NaCl–KCl–AlCl₃ or EMIC–AlCl₃ electrolytes. LSV scans were performed from the open circuit voltage (OCV) down to -35 mV versus OCV at a scanning rate of 10 mV s⁻¹. The thermodynamic studies were performed by running the cell at stepwise increasing temperatures, that is, 110 °C, 150 °C, 180 °C, 210 °C and 250 °C for the NaCl–KCl–AlCl₃ cell and 25 °C, 60 °C, 95 °C, 110 °C, 150 °C, 180 °C, 210 °C and 250 °C for the EMIC–AlCl₃ cell. A small range of voltage (35 mV) was used to avoid extensive progress of redox reactions and resistive surface layer build-up. The cells were conditioned at each temperature for one hour before measurements. At all temperatures measurements were performed on one cell (rather than multiple cells) to avoid errors arising from different cells. The exchange currents were extracted by linear fitting of the linear range of the Tafel plots derived from the LSV scan and using the intercept value with the OCV = 0 axis (Extended Data Fig. 1). Three scans were performed at each temperature so as to obtain the average values and standard errors.

The exchange current measured on an electrochemical cell is dictated by the reaction of the more sluggish electrode. In the Al|Al symmetric cells, the two electrodes undergo the same Al plating/stripping processes. In the Al|Se cells, Al plating/stripping (the same as that in the Al|Al cell) occurs at the negative electrode and selenium oxidation/reduction occurs at the positive electrode. On the basis of these assumptions and arguments, if one compares the exchange current of an Al|Al cell to that of an Al|Se cell with a fixed positive/negative capacity ratio, it is possible to identify the rate-limiting reaction, that is, the negative or positive electrode. For example, for the EMIC–AlCl₃ electrolyte, the exchange current of the Al|Se cell is 80% smaller than that of the Al|Al cell at 110 °C, meaning that the selenium reaction limits the rate at 110 °C.

To measure the ionic conductivity of the electrolytes, the electrochemical impedance spectrum (EIS) of an Al|Al cell was measured. The Nyquist plot at high frequency was fitted to a semicircle. The electrolyte resistance was found from the lower intercept with the real axis. The conductivity was calculated by use of a cell constant calibrated with the EMICEISAAlCl₃ electrolyte at 25 °C.

The AIMD simulations for the two electrolytes allow one to analyse the solvation structure around Al³⁺ and its desolvation energetics (detailed in the Methods). Clearly, the Al³⁺ prefers a tetrahedral coordination with Cl⁻ forming AlCl₄⁻ and Al₂Cl₇⁻ ions in both electrolytes (Fig. 1d and Extended Data Fig. 2a,b). The average coordination around Al³⁺, $Z(r)$, as a function of Al–Cl separation distance, r , calculated by integrating

the radial distribution functions, lends further statistical support to this coordination (Fig. 1e). The first coordination shell around Al³⁺ contains 4 Cl⁻ nearest neighbours in both cases (at $r = 2.1$ – 2.4 Å)⁴⁵. The most striking difference in the solvation structures between the two electrolytes is the formation of higher-order Al₃Cl₁₀⁻ in the NaCl–AlCl₃ melt (Fig. 1d,f); close examination of the AIMD trajectory also revealed the transient presence of Al₄Cl₁₃⁻. This is also reflected in the surge of Al neighbours around Al³⁺ at Al–Al separation distances of $r > 5$ Å (Fig. 1e). In NaCl–AlCl₃ melts at high AlCl₃ concentrations, which makes them strong Lewis acids⁴⁶, the polymerization of Al–Cl clusters is thermodynamically favourable and, importantly, is not kinetically hindered, as is the case in EMIC–AlCl₃ in which the huge EMI⁺ cation (elongated over 6 Å on its major axis as compared to Na⁺, which is spherically symmetric with a radius of 1 Å) impedes Cl⁻ hopping (Extended Data Fig. 2a,b and Supplementary Videos 1–4). The presence of higher-order Al_{*n*}Cl_{*3n+1*}⁻ ($n > 2$) in the alkali-chloroaluminate is experimentally confirmed by high-temperature Raman spectroscopy using an in-house-designed chamber (Fig. 1g and Extended Data Fig. 2d), which showed the presence of a peak at 176 cm⁻¹ (refs. 47,48) in addition to the bands representing AlCl₄⁻ and Al₂Cl₇⁻. The ²⁷Al nuclear magnetic resonance (NMR) spectroscopy performed at 90 °C on a high-entropy alkali-chloroaluminate melt MCl–AlCl₃ (LiCl:NaCl:KCl:AlCl₃ = 18:18:6:57, mol/mol; melting point around 75 °C) lends further support to the claim (see the detailed discussion in Extended Data Fig. 2e,f).

Electrochemical performance of the Al–Se battery

In molten NaCl–AlCl₃ at 180 °C the polarization is as small as 30 mV resulting in a high round-trip energy efficiency (96.5%). The cell with EMIC–AlCl₃ at 180 °C exhibits doubled polarization (70 mV). The GITT measurement shows a much-reduced overpotential for the NaCl–AlCl₃ cell owing to enhanced charge-transfer kinetics (Extended Data Fig. 5a,b, with further discussions). Nearer to room temperature the EMIC–AlCl₃ cells operate with much higher polarization and deliver much lower capacity with rapid fading (Fig. 2a and Extended Data Fig. 4g,h). The cell using molten NaCl–AlCl₃ shows decent cycling stability, sustaining 300 mAh g⁻¹ and no voltage decay over 50 cycles at rates of D/5 and C/2 (Extended Data Fig. 5c,d). We also observe similar stability for a cell fitted with a milled commercial selenium positive electrode (Extended Data Fig. 5e).

We evaluated the rate capability of Al–Se cells by varying the charging rates (from 0.5C to 200C) while discharging at a fixed D/10 rate, mimicking practical requirements (Fig. 2b and Extended Data Fig. 5f). The selenium shows a reversible capacity of 520 mAh g⁻¹ at a charging rate of C/2 and maintains a capacity of 190 mAh g⁻¹ at 10C. When the charging rate is increased by a factor of 400 from C/2 to 200C, the cell still retains a 75 mAh g⁻¹ capacity. Significantly, this is not an ion-adsorption capacitive behaviour, because both charge and discharge show well-defined plateau-like time traces and differential-capacity curves (Extended Data Fig. 5g,h). Only a marginal fraction of the capacity in the applied-voltage window comes from the carbon (Extended Data Fig. 4f). The faradaic behaviour at high rates is also confirmed by spectroscopic studies as discussed below. By contrast, the EMIC–AlCl₃ cell shows a capacity close to zero at charging rates exceeding 10C (Fig. 2b and Extended Data Fig. 5h).

Operando and ex situ XAFS measurements

The selenium for XAFS analysis, prepared by melt diffusion with nano-carbon, is non-crystalline (Extended Data Fig. 6a,b). Figure 3a shows the time-resolved Se K-edge X-ray absorption near-edge structure (XANES) spectra during the first discharge. With the SOD at 0–50%, the Se–K white line (12659 eV, 1s→4p transition) shows a slight shift towards higher energy with decreased intensity, indicating reduction of selenium⁴⁹ and cleavage of the Se–Se bond³⁴. Further discharge triggers an abrupt change of the spectrum with a substantially shifted white line (approximately 12,662 eV). The first few spectra share a single set of

isosbestic points, but the spectra towards the end of the discharge do not show any unique common intersection points (Fig. 3b and Extended Data Fig. 6c), clearly indicating more than two components are present. Our principal component analysis also confirms that a minimum of three components is required to describe the ensemble of spectra (Extended Data Fig. 6d–f), indicating the formation of intermediate selenium species. Using the multivariate curve resolution-alternating least-squares (MCR-ALS) method^{50,51}, we deconvolve the spectra (in both energy and frequency space) and identify the three possible components, noted as A (starting), B (intermediate), C (ending) (Fig. 3c and Extended Data Fig. 6g). A is confirmed to be elemental Se⁰; C is treated as the end member of the discharge and assigned as Al₂Se₃ (not Cl-coordinated compounds), based on the first-shell fitting of the EXAFS using paths derived from crystallographic data (detailed in Extended Data Figs. 6h–j and 7a–e). This agrees with our assertion that the Al³⁺ is fully desolvated before the reaction (reaction R-0). The EXAFS $k^2\chi(k)$ oscillation of B shows close profiling with C and A at high and low frequencies, respectively, implying the presence of both Se–Se and Se–Al coordination; the slight phase shift of B relative to C at low k indicates different Al–Se bonding distances in the two compounds (Fig. 3c). We tentatively assign B as Al₂(Se_n)₃ with the exact stoichiometry to be determined. Indeed, the best EXAFS fitting of B supports such coordination in the first shell (Fig. 3d, as detailed in Extended Data Fig. 7g–j).

The Se K-edge EXAFS experiments were carried out at the sector 20-BM-B in the Advanced Photon Source at Argonne National Laboratory, using a Si(111) crystal monochromator. A focused beam about the size of 500 × 500 μm² and 15% detuning was used. The XAFS data were collected in transmission mode. The samples/cells were placed in open air. The incident I_0 chamber (diameter = 15 cm) was under a constant flow of 50% N₂ and 50% He, and the transmission I_1 chamber (diameter 30 cm) was under a flow of 100% N₂. Energy calibration was established using selenium foil with the edge at 12,658.0 eV. A selenium foil was attached in front of I_{ref} , where I_{ref} is the X-ray intensity measured by an ion-chamber placed behind the selenium foil serving as the calibration standard to align each measurement.

The cell for operando XAFS was adapted from 2,032 coin cells that use Kapton (Sheldahl) windows on both sides of the cell case for incident and transmitted beams (24 mm thick, diameter 4 mm). A glassy carbon disk was placed between the Kapton window and the positive electrode to maintain uniform pressure throughout the electrode. A free-standing carbon paper (P50, Fuel Cell Earth) was used as the current collector. A thin Al foil (8 μm thick) was used as the negative electrode, along with a holed (diameter 4 mm for beam penetration) molybdenum foil negative electrode current collector. A Teflon gasket that is stable at 180 °C was used to seal the cell. The Na₂Se₂ standard material was synthesized by reacting sodium with naphthalene in tetrahydrofuran forming the Na radical, which was then reacted with selenium at the stoichiometric ratio. The tetrahydrofuran was then dried off in vacuo to yield the phase-pure Na₂Se₂. The ex situ measurements for the fast-charging studies were performed on selenium electrodes retrieved from the cycled laboratory Swagelok cells. The cells were discharged at a rate of D/10 and rapidly recharged at 20C and 50C, respectively. The cycled selenium electrodes, along with the separator and electrolyte, were sealed in a Kapton envelope for ex situ measurement.

About 80 mg of the NaCl–AlCl₃ electrolyte (with melt density of approximately 1.7 g cm⁻³) was used in each cell and the areal selenium loading was approximately 3 mg cm⁻². The thickness of all cell components along the beam path (including the two electrodes, electrolyte, glass fibre separator, aluminium foil, Kapton windows) was determined such that the total absorption length was lower than 2 for optimal statistics of the transmitted signal. The cell was heated using a temperature-controlled heating board. The cell was discharged at a rate of D/10 at 180 °C. For XAFS spectrum acquisition, we followed a pattern of three consecutive scans (at three different spots) and then

a 20 min pause. Each scan took 7 min so that the composition change between two spectra was about 8 mAh g⁻¹ (that is, 1.2% of the total capacity) at a cycling rate of D/10. The discharge of the cell and the XAFS data acquisition were not interrupted during cycling.

Athena software was used to calibrate, align and normalize the XAFS spectra⁵². The normalized spectra sets were analysed with principal component analysis in the energy space, and the minimal number of components that were required to describe the data set was determined such that they can describe 99.99% of the variance of the data. The predetermined number of components was also used as an input to the MCR-ALS analysis for mathematically determining the XAFS spectra feature of the components⁵⁰. In the MCR-ALS analysis, the singular value decomposition method was used to confirm the number of components; the non-negativity constraint of both the concentration and the spectra was applied. A convergence criterion of 0.01 was used for the optimization condition. Using energy or frequency space data as the input for the MCR-ALS analysis yields essentially the same results on the spectra. The reconstructed components were then used as standards for linear combination fitting of the spectra set (in energy space) to quantify the fraction of each component as a function of the SOD. The reduced χ^2 was used to evaluate the goodness of the fittings and to re-evaluate the number of components required in each scan (Extended Data Fig. 7d).

Quantitative curve fittings of the reconstructed components were performed for the Fourier-transformed $k^2\chi(k)$ in R space using Artemis software⁵². A k range of [4,14] Å⁻¹ was used for the Fourier transform and curve fittings were carried out within an R range of [1.3,2.5] Å using a k^3 weight. For the Se–Na path, an R range of [1.3,3] Å was used. The amplitude reduction factor (S_0^2) was determined by fitting the standard selenium sample using paths from the crystalline data; the S_0^2 was then fixed throughout all the fitting. In general, the coordination number (N , set positive), Debye–Waller factors (σ^2), bond length (R) and change in energy (ΔE_0) were all treated as adjustable parameters. The scattering paths utilized for the EXAFS fittings were taken from the crystalline phases calculated by the free energy force field (FEFF), as shown in Extended Data Figs. 5–7. We have made a number of attempts on fitting each component using possible Se coordination(s), to resolve the best fit with confidence.

Operando XRD measurements

Operando XRD measurements were carried out using a PANalytical Empyrean diffractometer fitted with a PIXcel detector. The diffraction patterns were collected using Cu K α radiation in Bragg–Brentano geometry. The ball-milling prepared selenium–carbon composite (70 wt% selenium) with high crystallinity was used to prepare the positive electrode. The electrode was coated on glassy carbon, which served both as the current collector and window. The cylinder cell was heated using a heating jacket during the measurement. The cell was discharged at a rate of D/10 with a pattern collection time of 18 min (22–32°, step size 0.013°).

In situ EIS measurements

The in situ EIS measurement was performed periodically under open circuit conditions at different states of discharge of the cell. Specifically, a current pulse of D/10 was sustained for 30 min, followed by 30 min OCV to reach quasi-equilibrium, at which point the EIS was measured; this was repeated until the completion of the discharge. The frequency was scanned over the range spanning 20 kHz to 20 mHz with an a.c. amplitude of 5 mV. An integration period of 1 s per sample and a measurement rate of 1 sample per second was used. The data at high frequency (20 kHz to 0.2 Hz) in the Nyquist plot were fitted to a semicircle to approximate the charge-transfer process; the charge-transfer resistance R_{ct} is derived from the difference between the two intercepts of the semicircle with real axis. The lower intercept with the real axis is assigned the value of the electrolyte resistance. Equivalent-circuit fitting was not attempted because the shape of the Nyquist plots varies with the state of charge as

the discharge proceeds; hence, it is difficult to find an equivalent circuit that represents all. For instance, the appearance of low-frequency long tails at the end of the discharge indicates a diffusion-limited process. The EIS and cycling measurements were conducted using Solartron XM-studio, and the data were analysed in the XM-studio ECS.

Physicochemical characterizations

The scanning-electron-microscopy imaging and energy-dispersive spectroscopy was performed on a Zeiss Merlin microscope. The Al deposits were retrieved from cycled cells and washed twice using acetonitrile solvent. The high-temperature Raman spectroscopy was performed on a HORIBA HR EVO Raman system using an in-house-designed air-tight sapphire-window chamber with controlled heating capability. The temperature was controlled at 180 °C. The high-temperature ²⁷Al NMR spectroscopy was performed on a Bruker 500 MHz instrument at 90 °C. Low-pressure air-tight sealed NMR tubes (Wilmad 528-LPV-7) were used to prevent the sample from being exposure to air and to maintain the pressure at high temperature in the NMR instrument. The electrolytes were loaded in an Ar-filled glovebox with O₂ and H₂O content below 0.1 ppm. A 1.1 M Al(NO₃)₃·9H₂O solution in deuterated water was used as the external reference (chemical shift set at 0 ppm). The electrolytes were not mixed with any deuterated solvent to avoid any magnetic interference and/or chemical reactions. The sealed electrolytes were preheated and melted in an oven, then transferred to the NMR chamber and held at 90 °C for 30 min before data acquisition. The measurement was performed twice within a 10 min interval to confirm that the electrolyte was stabilized at the target temperature. The transmission-electron-microscopy images were taken on a JEM-2100F-STEM microscope. The ex situ XRD measurement was carried out on a PANalytical X'Pert PRO XRPD system. For thermogravimetric analysis of the electrolytes, the ionic liquid or molten salt was loaded into an aluminium crucible and sealed under Ar to reduce exposure during sample transfer. The sealed crucible was pierced right before measurement to let out any gas evolved from the analysis. The measurement was performed on a NETZSCH STA 449 F3 thermal analyser.

AIMD simulations of the electrolyte

All the AIMD simulations were performed within the framework of density functional theory (DFT) using the projector-augmented-wave formalism in the Vienna Ab initio Simulation Package (VASP)^{53,54}. Using the generalized gradient approximation, we simulated two electrolyte systems: EMIC–AlCl₃ (2:3 molar) and NaCl–AlCl₃ (2:3 molar) to complement the experiments. We used the pseudopotentials provided by VASP, and described the exchange correlation using Perdew–Burke–Ernzerhof functional⁵⁵. The computational supercell in each case consisted of approximately 350 atoms (17 × 17 × 17 Å³ for EMIC–AlCl₃ and 21 × 21 × 21 Å³ for NaCl–AlCl₃) with densities close to experimentally measured values; periodic boundary conditions were used along all directions to simulate bulk electrolytes. The initial configurations of the electrolytes were prepared by placing EMIC/NaCl/AlCl₃ molecules at random locations and arbitrarily chosen orientations within the supercell. Long-range van der Waals dispersion interactions were treated using the DFT-D2 method⁵⁶. The plane-wave-energy cutoff was set at 520 eV and the Brillouin zone was sampled at the Γ point only. Each electrolyte system was equilibrated at 180 °C in the canonical ensemble (NVT) for 30 ps, wherein constant temperature conditions were maintained by is of a Nose–Hoover thermostat. A timestep of 0.5 fs was used to integrate the equations of motion. The structure of the electrolyte was determined by averaging the configurations over the last 10 ps of the AIMD trajectories. The diffusivity of ions was derived from the mean square displacement calculated over a longer run of 40 ps.

Calculations of desolvation energetics

We used gas-phase DFT quantum-chemical cluster calculations as implemented in the Gaussian 09 code⁵⁷ to understand the energetics

of desolvation of Al³⁺ from various chloroaluminate clusters. The chloroaluminate anion clusters (that is, AlCl₄⁻, Al₂Cl₇⁻ and Al₃Cl₁₀⁻) obtained from AIMD simulations were used as starting configurations for the quantum-chemical calculations. In each of these cases, the long-range corrected hybrid functional, ω B97x-D⁵⁸, with 6–31+G(d,p) basis set was used to optimize the geometry and to evaluate the electronic energy (*E*), enthalpy (*H*) and Gibbs free energy (*G*) in the gas phase.

Data availability

The datasets analysed and generated during the course of this study are included in the paper and its Supplementary Information.

- Kendall, J., Crittenden, E. D. & Miller, H. K. A study of the factors influencing compound formation and solubility in fused salt mixtures. *J. Am. Chem. Soc.* **45**, 963–996 (1923).
- Midorikawa, R. Studies on electrolytic refining of aluminum at low temperature in aluminum chloride baths. IV. Measurement of the densities of the ternary molten salts AlCl₃–NaCl–KCl. *Denki Kagaku* **23**, 352–355 (1955).
- Wei, S. et al. Metal-sulfur battery cathodes based on PAN-sulfur composites. *J. Am. Chem. Soc.* **137**, 12143–12152 (2015).
- Salanne, M., Siqueira, L. J. A., Seitonen, A. P., Madden, P. A. & Kirchner, B. From molten salts to room temperature ionic liquids: simulation studies on chloroaluminate systems. *Faraday Discuss.* **154**, 171–188 (2012).
- Heerman, L. & D'Olieslager, W. Potentiometric study of the solvent equilibria in AlCl₃–N-n-butylpyridinium chloride melts. *Inorg. Chem.* **24**, 4704–4707 (1985).
- Øye, H. A. & Rytter, E. Raman spectra of KCl–AlCl₃ melts and normal coordinate analysis of Al₃Cl₁₀⁻. *Acta Chem. Scand.* **25**, 559–576 (1971).
- Rytter, E., Øye, H. A., Cyvin, J., Cyvin, B. N. & Klæboe, C. P. Raman spectra of AlCl₃–AlkCl and trends in species formation. *J. Inorg. Nucl. Chem.* **35**, 1185 (1973).
- Gao, J., Lowe, M. A., Kiya, Y. & Abruña, H. D. Effects of liquid electrolytes on the charge-discharge performance of rechargeable lithium/sulfur batteries: electrochemical and in-situ X-ray absorption spectroscopic studies. *J. Phys. Chem. C* **115**, 25132–25137 (2011).
- de Juan, A. & Tauler, R. Chemometrics applied to unravel multicomponent processes and mixtures: revisiting latest trends in multivariate resolution. *Anal. Chim. Acta* **500**, 195–210 (2003).
- Broux, T. et al. VIV disproportionation upon sodium extraction from Na₃V₂(PO₄)₂F₃ observed by operando X-ray absorption spectroscopy and solid state NMR. *J. Phys. Chem. C* **121**, 4103–4111 (2017).
- Ravel, B. & Newville, M. ATHENA, ARTEMIS, HEPHAESTUS: data analysis for X-ray absorption spectroscopy using IFFFIT. *J. Synchrotron Radiat.* **12**, 537–541 (2005).
- Kresse, G. & Furthmüller, J. Efficient iterative schemes for ab initio total-energy calculations using a plane-wave basis set. *Phys. Rev. B* **54**, 11169–11186 (1996).
- Kresse, G. & Joubert, D. From ultrasoft pseudopotentials to the projector augmented-wave method. *Phys. Rev. B* **59**, 1758–1775 (1999).
- Perdew, J. P., Burke, K. & Ernzerhof, M. Generalized gradient approximation made simple. *Phys. Rev. Lett.* **77**, 3865–3868 (1996).
- Harl, J., Schimka, L. & Kresse, G. Assessing the quality of the random phase approximation for lattice constants and atomization energies of solids. *Phys. Rev. B* **81**, 115126 (2010).
- Frisch, M. J. et al. Gaussian 09, Revision E.01 (Gaussian, Inc., 2009).
- Chai, J.-D. & Head-Gordon, M. Long-range corrected hybrid density functionals with damped atom–atom dispersion corrections. *Phys. Chem. Chem. Phys.* **10**, 6615–6620 (2008).
- Cleaver, B. & Koronaios, P. Viscosity of the NaCl⁺ AlCl₃ melt system, including the effect of added oxide. *J. Chem. Eng. Data* **39**, 848–850 (1994).
- Zheng, Y., Zheng, Y., Wang, Q., Wang, Z. & Tian, D. Density and viscosity of binary mixtures of 1-ethyl-3-methylimidazolium heptachlorodialuminate and tetrachloroaluminate ionic liquids. *J. Chem. Eng. Data* **62**, 4006–4014 (2017).
- Wilkes, J. S., Levisky, J. A., Wilson, R. A. & Hussey, C. L. Dialkylimidazolium chloroaluminate melts: a new class of room-temperature ionic liquids for electrochemistry, spectroscopy and synthesis. *Inorg. Chem.* **21**, 1263–1264 (1982).
- Wilkes, J. S., Frye, J. S. & Reynolds, G. F. Aluminum-27 and carbon-13 NMR studies of aluminum chloride-dialkylimidazolium chloride molten salts. *Inorg. Chem.* **22**, 3870–3872 (1983).
- Tauler, F. & Popov, A. I. Aluminum-27 NMR study of some AlCl₃⁻ MCl molten systems. *J. Solut. Chem.* **15**, 463–471 (1986).
- Nakayama, Y. et al. Sulfone-based electrolytes for aluminium rechargeable batteries. *Phys. Chem. Chem. Phys.* **17**, 5758–5766 (2015).
- Angell, M. et al. High Coulombic efficiency aluminum-ion battery using an AlCl₃-urea ionic liquid analog electrolyte. *Proc. Natl Acad. Sci. USA* **114**, 834–839 (2017).
- Kravchuk, K. V., Wang, S., Piveteau, L. & Kovalenko, M. V. Efficient aluminum chloride–natural graphite battery. *Chem. Mater.* **29**, 4484–4492 (2017).
- Schneider, H. et al. On the electrode potentials in lithium-sulfur batteries and their solvent-dependence. *J. Electrochem. Soc.* **161**, A1399 (2014).
- Kaplan, L. H. & d'Heurle, F. M. The deposition of molybdenum and tungsten films from vapor decomposition of carbonyls. *J. Electrochem. Soc.* **117**, 693 (1970).
- Kılıçaslan, A. et al. Hard titanium nitride coating deposition inside narrow tubes using pulsed DC PECVD processes. *Surf. Coat. Tech.* **377**, 124894 (2019).
- Yin, et al. Faradaically selective membrane for liquid metal displacement batteries. *Nat. Energy* **3**, 127–131 (2018).

71. Nelson, P. A., Ahmed, S., Gallagher, K. G. & Dees, D. W. *Modeling the Performance and Cost of Lithium-Ion Batteries for Electric-Drive Vehicles*, 3rd edn (Argonne National Laboratory, 2019); <https://doi.org/10.2172/1503280>.
72. Eroglu, D., Zavadil, K. R. & Gallagher, K. G. Critical link between materials chemistry and cell-level design for high energy density and low cost lithium-sulfur transportation battery. *J. Electrochem. Soc.* **162**, A982–A990 (2015).
73. Berg, E. J., Villevieille, C., Streich, D., Trabesinger, S. & Novak, P. Rechargeable batteries: grasping for the limits of chemistry. *J. Electrochem. Soc.* **162**, A2486–A2475 (2015).
74. Liao, Q., Sun, B., Liu, Y., Sun, J. & Zhou, G. A techno-economic analysis on NaS battery energy storage system supporting peak shaving. *Int. J. Energy Res.* **40**, 241–247 (2016).
75. Boston, C. R. Density of molten AlCl_3 and NaCl-AlCl_3 mixtures. *J. Chem. Eng. Data* **11**, 262–263 (1996).
76. Matiašovský, K., Fellner, P. & Chrenková-Paučířová, M. Density and electrical conductivity of molten NaCl-KCl-AlCl_3 mixtures. *Electrochim. Acta* **25**, 195–200 (1980).

Acknowledgements We acknowledge financial support from the MIT Energy Initiative, the MIT Deshpande Center for Technological Innovation and ENN Group. Q.P., J.M. and X.H. thank the Peking University startup funding, the National Natural Science Foundation of China (grant no. 22075002) and National Postdoctoral Programme for Innovative Talents (grant no. BX2021002). L.M. acknowledges financial support from The National Key Research and Development Program of China (grant no. 2020YFA0715000). B.N. and S.G. acknowledge funding from the Office of the Executive Vice President for Research and Innovation at University of Louisville. This research used resources of the National Energy Research Scientific Computing Center, a DOE Office of Science User Facility supported by the Office of Science of the US Department of Energy under Contract No. DE-AC02-05CH11231. This research used resources of the Advanced Photon Source, an Office of Science User Facility

operated for the US Department of Energy (DOE) Office of Science by Argonne National Laboratory and was supported by the US DOE under Contract No. DE-AC02-06CH1135. We are grateful for discussions of the cost analysis with L. Ortiz.

Author contributions Q.P. and D.R.S. conceived the concept. Q.P. designed the experimental work. B.N. and Q.P. designed the computational work and proposed the desolvation mechanism. Q.P. and M.B. designed the synchrotron work. Q.P. and J.M. prepared the electrolytes and performed physical characterizations and electrochemical measurements with the help of X.H., J.Z., Y.J., L.X., S.T., Z.W., O.K. and L.M. S.G. carried out the computational work under the supervision of B.N. C.Y.K. and Q.P. performed the operando XRD studies with the supervision of L.F.N. Q.P. conducted the XAFS data collection and analysis with help from J.M. and under the supervision of M.B. Q.P. and D.R.S. drafted the manuscript with contributions from L.F.N., M.B., B.N. and all co-authors. D.R.S. supervised the work.

Competing interests D.R.S. is a co-founder of Avanti Battery Co., a company established to commercialize the aluminium–sulfur battery. D.R.S.'s role with the company is advisory; he is formally the Chief Scientific Advisor.

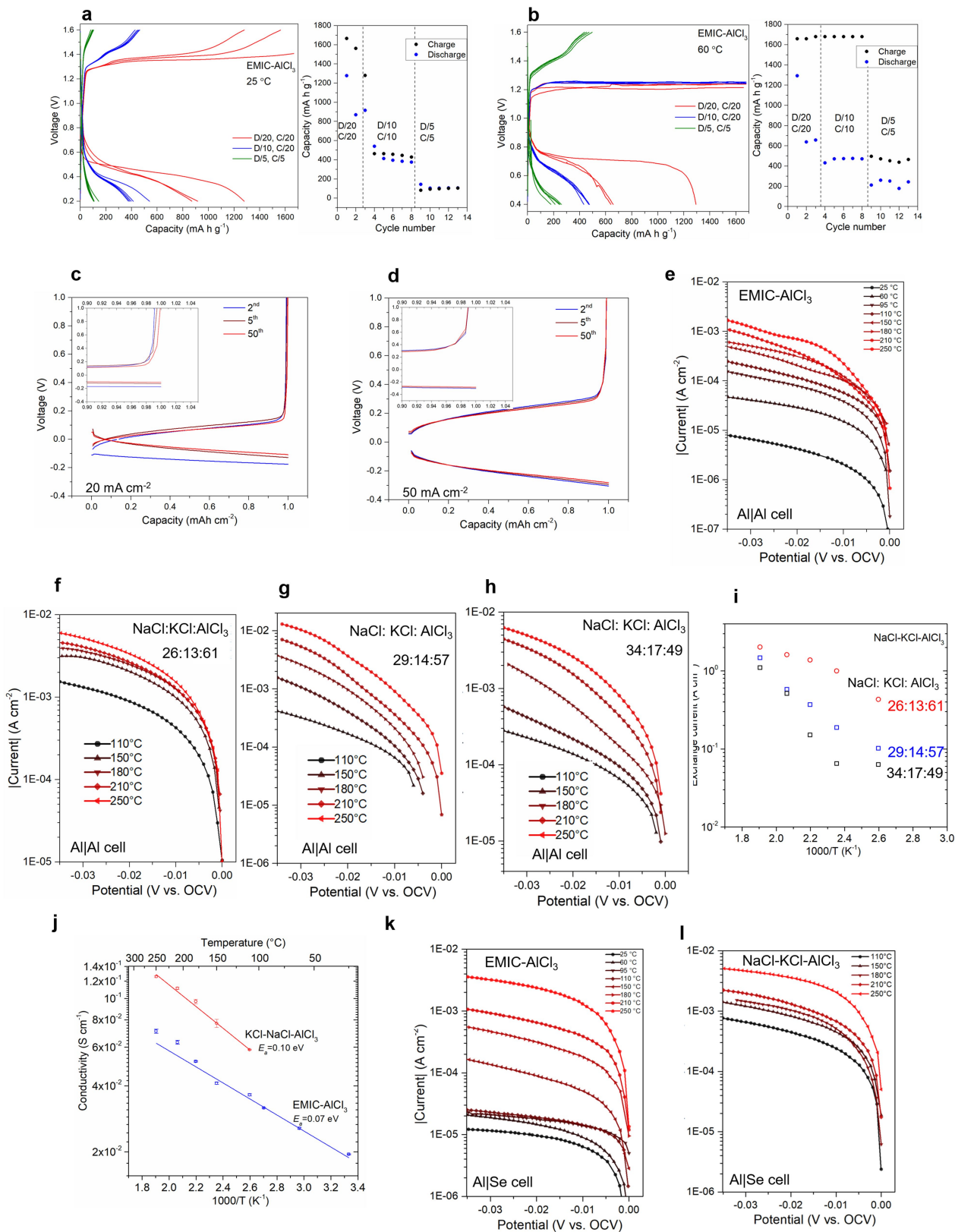
Additional information

Supplementary information The online version contains supplementary material available at <https://doi.org/10.1038/s41586-022-04983-9>.

Correspondence and requests for materials should be addressed to Quanquan Pang or Donald R. Sadoway.

Peer review information *Nature* thanks George Chen, Robert Dominko and Feng Li for their contribution to the peer review of this work. Peer reviewer reports are available.

Reprints and permissions information is available at <http://www.nature.com/reprints>.



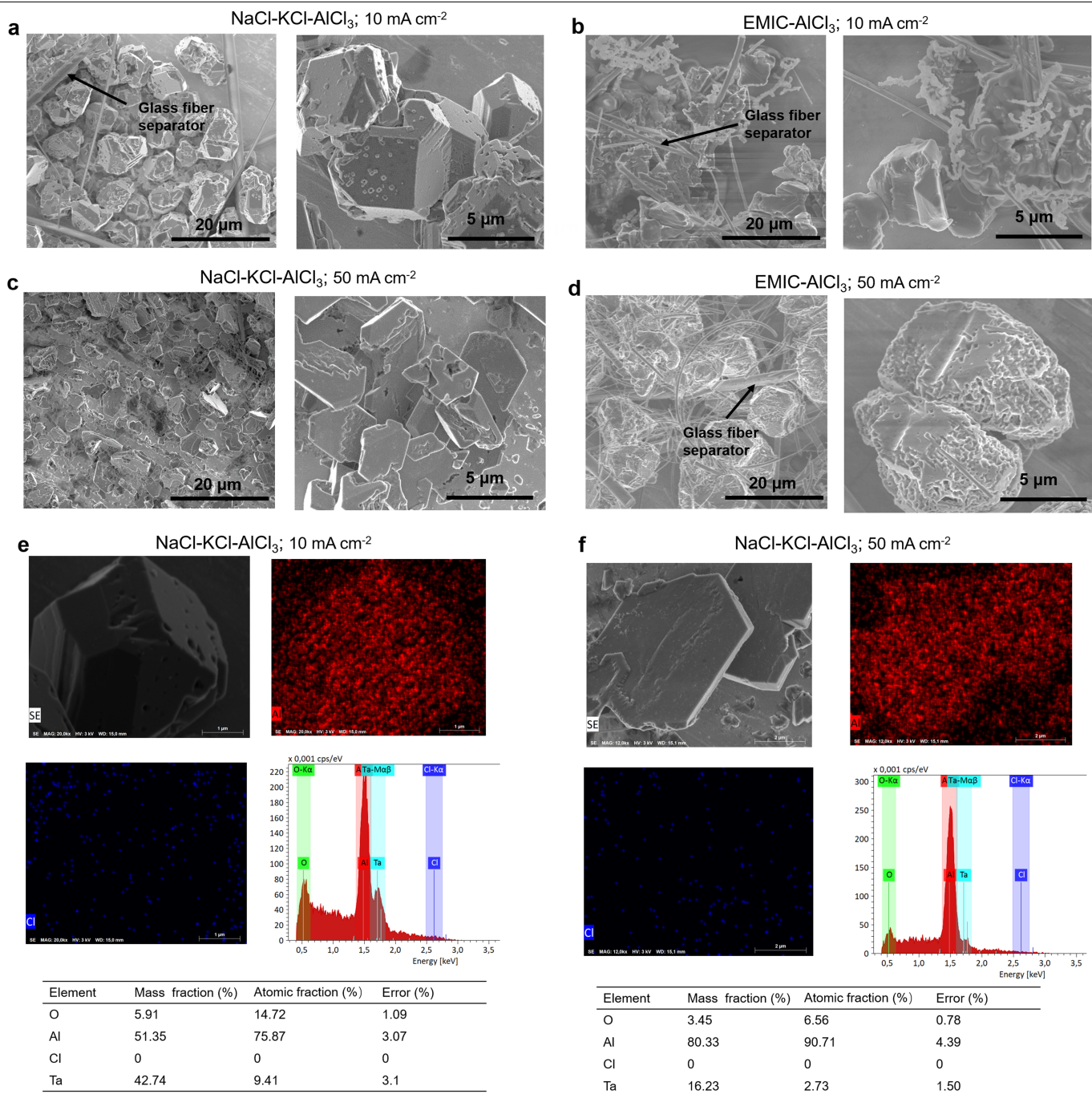
Extended Data Fig. 1 | See next page for caption.

Extended Data Fig. 1 | The fundamental electrochemical behavior of the chloroaluminate melt electrolytes. a, b, The discharge/charge voltage-time traces and the rate capability of Al-S batteries in the widely reported EMIC-AlCl₃ electrolyte at 25 °C (**a**) and 60 °C (**b**). The batteries use graphene/sulfur as the positive electrode. Ionic-liquid cells show low discharge voltage (0.5V) and very large polarization even at the low rates of D/20, C/20 at 25 °C. **c, d,** The Al plating/stripping coulombic efficiency measurements using an Al|Ta symmetric cell configuration in the molten NaCl-KCl-AlCl₃ electrolyte at a current density of (**c**) 20 mA cm⁻² and (**d**) 50 mA cm⁻² at 180 °C (the insets are the expanded view). **e-h,** the linear-sweep voltammetry (LSV) of Al|Al symmetric cells at different temperatures in EMIC-AlCl₃ (**e**) and NaCl-KCl-AlCl₃ with varied molar ratios (**f-h**); **i,** The logarithmic plot of the temperature-dependent exchange current of Al|Al symmetric cells in NaCl-KCl-AlCl₃ with varied molar ratios. It is clear that as the electrolyte becomes more basic (higher percentage

of alkali chloride), the exchange current I_0 decreases. In another word, even with the same type of cations, the exchange current varies with composition, i.e., with Lewis acidity. Therefore, it is not the cationic component, but rather the anionic cluster component (which is affected by the choice of cations and the instant concentration = Lewis acidity) that fixes the higher I_0 observed in the NaCl-KCl-AlCl₃ system. **j,** The logarithmic plot of ionic conductivity as a function of temperature, where the activation energy E_a is derived assuming Arrhenius behavior. **k, l,** The LSV curves of Al|Se cells at different temperatures in NaCl-KCl-AlCl₃ (**f**) and EMIC-AlCl₃ (**g**) electrolytes. In all LSV plots, the voltage is expressed as the potential v_s the open circuit voltage of the cell. For exchange current calculation, regression fitting of the linear part of the LSV curves was performed and the intercept of the fitted line with the $V = 0$ voltage is assigned to be the exchange current.

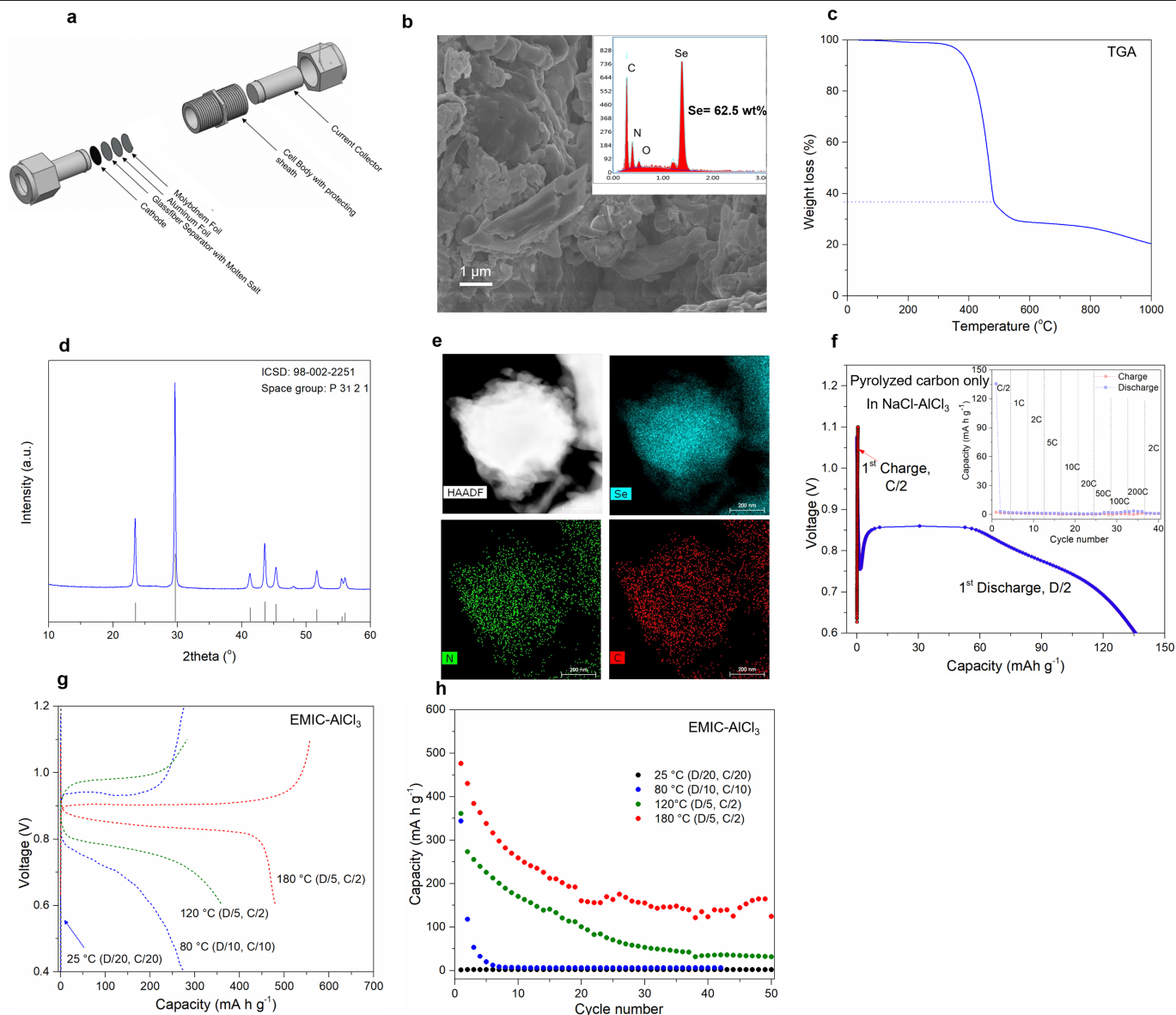
Extended Data Fig. 2 | Experimental and computational studies of the chloroaluminate melts. **a, b**, Typical snapshots from the AIMD trajectories for the two electrolytes EMIC- AlCl_3 (**a**) and NaCl-AlCl_3 (**b**); Carbon (grey), hydrogen (white), and nitrogen (blue), and sodium (green) are displayed here to highlight the steric effects of the giant EMI^+ cations in the EMIC- AlCl_3 electrolyte. The Cl^- , AlCl_4^- , Al_2Cl_6 , Al_2Cl_7^- , and $\text{Al}_3\text{Cl}_{10}^-$ clusters are shown in purple, dark blue, gold, cyan and red respectively. **c**, The diffusivity of each ion calculated based on the mean square displacement derived from the AIMD simulations over a long duration of 40 ps. **d**, The schematic illustration of our house-designed high-temperature Raman chamber. **e, f**, The ^{27}Al NMR spectra of the two electrolytes (**e**) and the deconvolution of the spectrum for the MCl-AlCl_3 electrolyte (**f**). **g-j**, The configuration of the clusters, and the scheme of proposed first step dissociation reaction to form Al_2Cl_6 for Al^{3+} de-solvation (equations 1–4), assuming breaking of the relatively longer Al-Cl bonds, for AlCl_4^- (**g**), Al_2Cl_7^- (**h**), $\text{Al}_3\text{Cl}_{10}^-$ (**i**), $\text{Al}_4\text{Cl}_{13}^-$ (**j**). Note that two AlCl_3 moieties (instead of one Al_2Cl_6) are shown here as the product for explicit illustration of the bond breaking scheme. QC calculations do support that one Al_2Cl_6 is more stable than two isolated AlCl_3 molecules. **k**, A schematic illustration of how the counter ions (Na^+ vs EMI^+) can impact the coulombic pulling of the Cl^{6-} away from the Al_2Cl_7^- cluster which in turn affects the ease of Al-Cl bond breaking and ultimately the Al^{3+} de-solvation kinetics. Apparently, the smaller (thus more localized charge) and closer Na^+ (as seen in the coordination plot in Fig. 1e) shows higher coulombic attraction for the Cl^{6-} within the cluster, based on Coulomb's law. **l**, The configuration of the Al_2Cl_6 cluster and the scheme of proposed dissociation of Al_2Cl_6 and eventual Al^{3+} de-solvation, along with the overall equations for all clusters. In the configuration panels, the Al and Cl atoms are shown as brown and purple spheres, respectively. The overall reactions for the desolvation of one Al^{3+} out of the clusters are shown in **i**. To add further experimental proof of the presence of $\text{Al}_n\text{Cl}_{3n+1}^-$ species ($n > 2$), we performed the high-temperature Raman spectroscopy on the NaCl-KCl-AlCl_3 electrolyte using a house-designed air-tight sapphire-window chamber with controlled heating capability. The measurement was performed at 180 °C and further experimental details are described in the Methods sections. We do note that owing to the intense fluorescence effect from the highly concentrated Cl ions, there is a high Raman background that compromises the signal/noise ratio; but we do clearly perceive the Raman bands of interest. We observe that in addition to the Raman bands corresponding to AlCl_4^- (centered at 351, 184, 122 cm^{-1}) and Al_2Cl_7^- (centered at 312, 160 and 110 cm^{-1}), the electrolyte shows an additional peak at 176 cm^{-1} , which can be ascribed to higher-order polyatomic clusters, i.e.

$\text{Al}_n\text{Cl}_{3n+1}^-$ ($n > 2$)^{47,48}. This clearly proves the existence of $\text{Al}_n\text{Cl}_{3n+1}^-$ ($n \geq 3$). Due to the temperature limit related to the detector of our NMR instrument, the measurements was performed at 90 °C, the highest temperature permitted. To specifically meet the temperature requirement, a high-entropy alkali chloroaluminate melt MCl-AlCl_3 ($\text{M} = \text{Li} + \text{Na} + \text{K}$, $\text{M}:\text{Al} = 1.31$; m.p. = -75 °C). The electrolytes were not mixed with any deuterated solvent to avoid any magnetic interference and/or chemical reactions. First, we observe that the ^{27}Al NMR spectrum of the alkali MCl-AlCl_3 shows a much broader peak, spanning from 135 ppm to 70 ppm (over 65 ppm), centered at a nominal chemical shift of 101.58 ppm, in comparison to that of the EMIC- AlCl_3 , centered at 103.54 ppm (nominal peak width: 1300 Hz vs. 313 Hz). For the EMIC- AlCl_3 , the two narrow peaks at 103.54 and 95.5 ppm can be respectively ascribed to AlCl_4^- and Al_2Cl_7^- . We stress that the much greater peak broadness cannot be ascribed to any difference in the viscosity of the liquids as they are reported to be rather close: around 7.69 mPa s for a NaCl-AlCl_3 (2:3) electrolyte at 90 °C⁵⁹, and 5.28 mPa s for an EMIC- AlCl_3 (2:3) electrolyte at 80 °C⁶⁰, nor to any difference in the Al ion concentration, as the $\text{MCl}:\text{AlCl}_3$ ratio is the same (2:3). Therefore, the much broader peak for MCl-AlCl_3 electrolyte can only be accounted for by the presence of multiple Al-cluster species which are in fast chemical exchange. We attempted to deconvolve the spectrum of the alkali MCl-AlCl_3 with a minimal number of peaks that show reasonable peak width (800-1250 Hz) using the linear fitting approach. The fitting clearly shows three peaks – any combination of two peak yields very large fitting residual. We note that in the literature, although there is universal agreement on the chemical shift of AlCl_4^- (around 103 ppm), the assignment for Al_2Cl_7^- is still unsettled^{61–66}, and there is no report on assignment for $\text{Al}_n\text{Cl}_{3n+1}^-$ ($n > 2$), to the best of our knowledge. Also, these reported assignments are exclusively based on room-temperature organic chloroaluminate ionic liquids, and not on high-temperature inorganic alkali chloroaluminate molten salts. Therefore, herein we take great caution when assigning the peaks. The two peaks at 103.6 ppm are ascribed to AlCl_4^- , while the higher field peak at 100.3 ppm is assigned to Al_2Cl_7^- . This assignment stands on the basis that the Al nuclei in Al_2Cl_7^- (i.e. a longer-chain $\text{Al}_n\text{Cl}_{3n+1}^-$) are more electron-shielded, intuitively due to the replacement of one electron-attracting Cl⁻ ligand with a less polarizable AlCl_4^- (see the molecular structure in Fig. 1f). Following this chemical principle, we tentatively ascribe the peak at the highest field of 94.4 ppm to $\text{Al}_n\text{Cl}_{3n+1}^-$ ($n > 2$). Note that the difference of the chemical shifts of Al_2Cl_7^- in the MCl-AlCl_3 compared to that in the EMIC- AlCl_3 is probably due to the vastly different coulombic interaction of the counter cations (M^+ vs EMI^+).



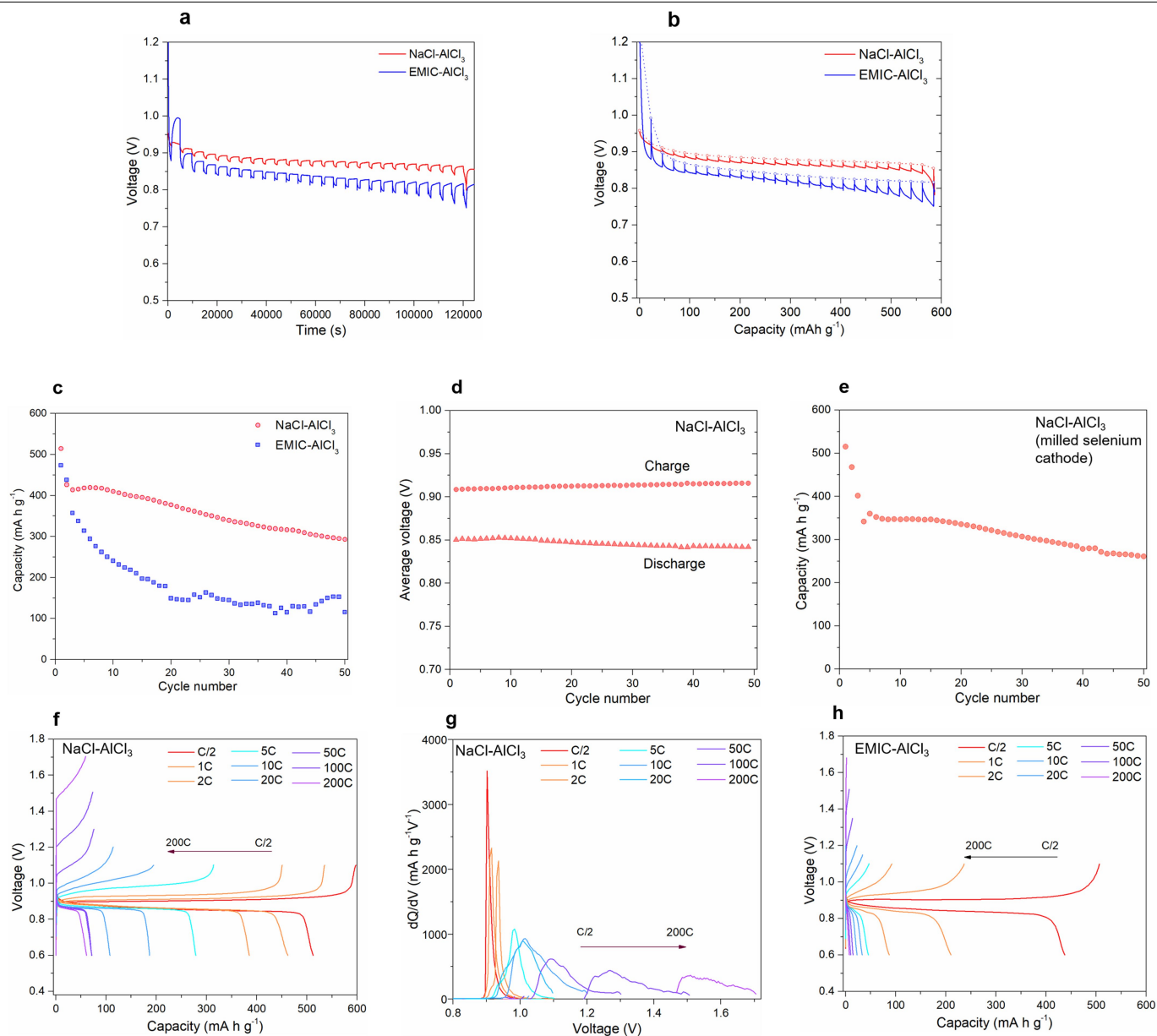
Extended Data Fig. 3 | Morphological and elemental characterization of the Al plating in the chloroaluminate electrolytes. **a-d**, The SEM images of Al plated on a Ta substrate at 180 °C in the NaCl-KCl-AlCl₃ electrolytes (**a,c**) and in the EMIC-AlCl₃ electrolyte (**b,d**) at a current density of 10 mA cm⁻² (**a,b**) and 50 mA cm⁻² (**c,d**) for an areal capacity of 5 mAh cm⁻². **e, f**, The SEM images and the corresponding EDX mapping (Al, Cl), EDX spectra, and the quantified

elemental compositions of plated Al (on a Ta substrate) performed in the NaCl-KCl-AlCl₃ electrolyte at a current density of 10 mA cm⁻² (**e**) and 50 mA cm⁻² (**f**) for an areal capacity of 5 mAh cm⁻². The EDX spectra and mapping show that to the resolution and detection limit of our EDX detector there is no Cl in the Al, which implies that the electrodeposit is pure Al metal containing no entrained electrolyte.



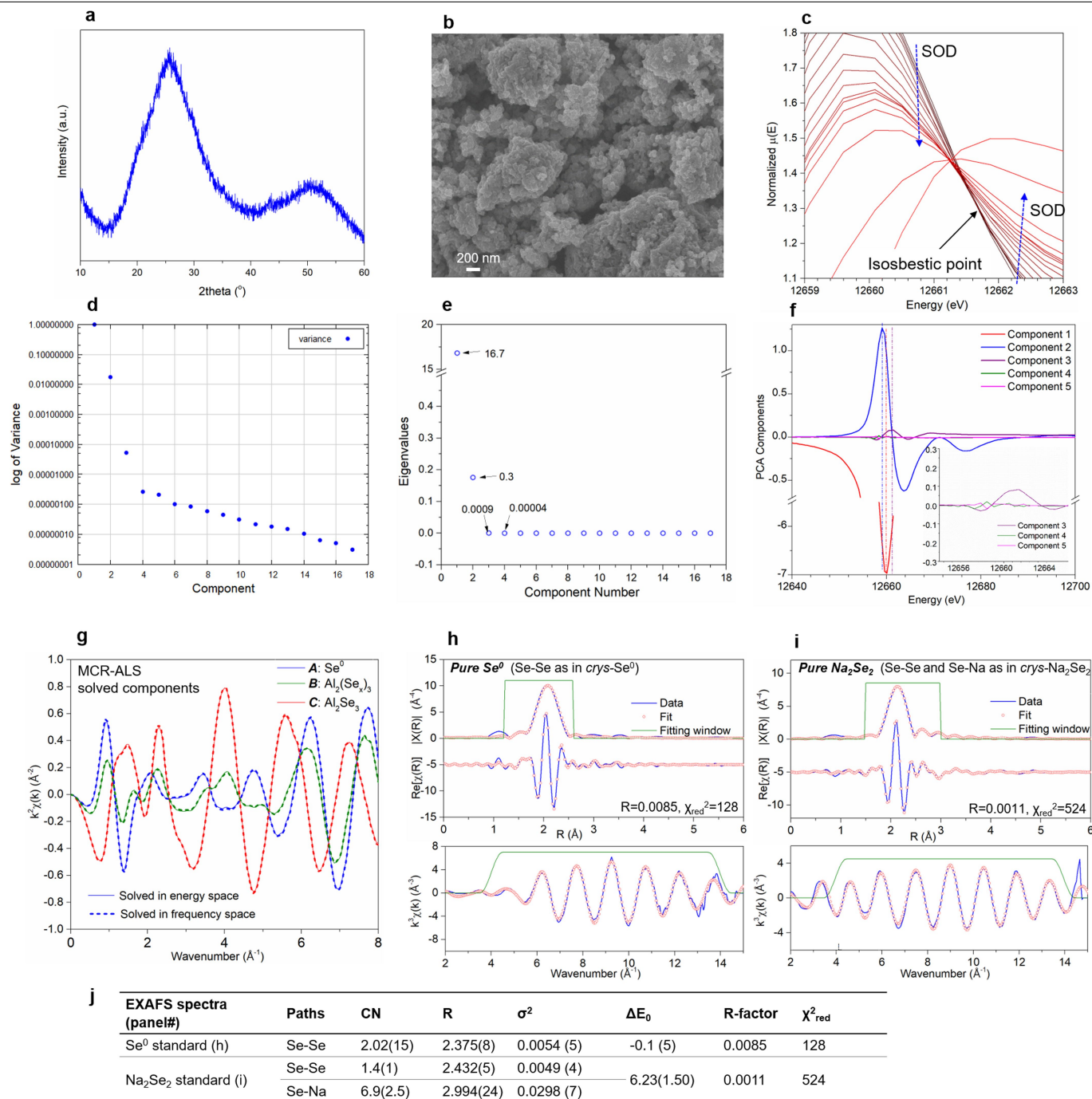
Extended Data Fig. 4 | Cell design and the physical and electrochemical characterizations of Te and Se electrodes. **a**, Schematic drawing of our in-house-made cell. **b-e**, Scanning electron microscopy image and energy-dispersive spectroscopy (EDS) (**c**), thermogravimetric analysis (**d**), X-ray diffraction pattern (**e**), transmission electron microscopy and EDS mapping (Se, N, C) (**b**) of the Se composite prepared by pyrolysis of polyacrylonitrile/selenium. The weight fraction of selenium in this composite is confirmed to be ~62.5% from both EDS and TGA analysis. The selenium

composite has a uniform distribution of Se, N and C, where the N is from the residue of pyrolyzed polyacrylonitrile. **f**, The first-cycle voltage-time trace and rate performance (varying charging rate and constant discharge at D/10) of the Se-free carbon material, prepared in the same way except without selenium. **g, h**, Voltage-time traces (**g**) capacity retention (**h**) of Se in EMIC-AlCl₃ at different temperatures and cycling rates, characterized by low capacity and fast fading even at very low cycling rates.



Extended Data Fig. 5 | Electrochemical behavior of Al-Se cells fitted with molten chloroaluminate electrolytes. (a) The GITT discharge voltage-time traces of Se electrodes (milled bulk selenium) in the two representative electrolytes, as a function of (a) measuring time and (b) of the specific capacity; measurement was performed with 20 min discharge at a C/5 rate followed by 1 h at rest; the equilibrium voltage is shown by circles in b. c. Capacity retention (discharge capacity) of Al-Se cells at rates of D/5 and C/2. d. Cell voltage (discharge and charge) as a function of cycle number for Al-Se cell running NaCl-AlCl₃ electrolyte. e. Capacity retention (discharge capacity) of an Al-Se cell using ball-milled bulk Se cathode with molten NaCl-AlCl₃. f, g. Voltage-time traces (f) differential capacity plots (dQ/dV) (g) of the Al-Se cells with molten NaCl-AlCl₃ at different charging rates and constant discharge at D/10. h. Voltage-time traces of an Al-Se cell in EMIC-AlCl₃ at different charge rates and constant discharge at D/10. The capacity and voltage time traces are determined by both the thermodynamic and kinetic factors. The GITT measurement allows one to answer what leads to the lower discharge capacity of the EMIC-AlCl₃ cell. To avoid any effect of the pyrolyzed polyacrylonitrile on the potential profile, we used a bulk selenium/carbon composite without special treatment. Extended Data Fig. 5a shows that the EMIC-AlCl₃ cell exhibits

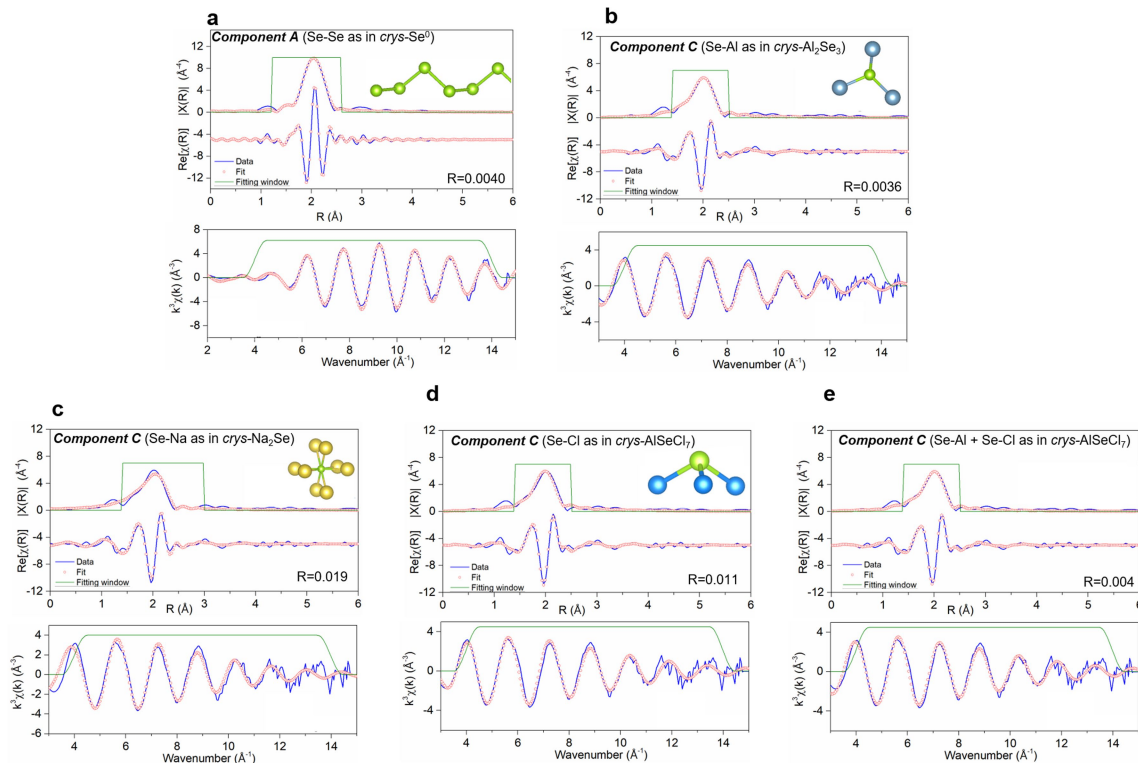
about the same capacity as the NaCl-AlCl₃ cell; as the GITT measurement allows a close to equilibrium reaction, it is clear that the lower discharge capacity measured in galvanostatic mode (as in Fig. 2a) is due to the kinetics. Indeed, this is further supported by the fact that the voltage difference between the end of discharge pulse and the end of equilibrium period, that is, the overpotential is larger in the EMIC-AlCl₃ cell than that in the NaCl-AlCl₃ cell (Extended Data Fig. 5a, b). This is particularly true at high depth of discharge. Further, the quasi-equilibrium voltage time traces of the two cells are slightly different, which indicates slightly different thermodynamic energetics of the reactions. This can be explained by the different solvation energies and/or solubility for the Al₂(Se_n)₃ intermediates by the different ions in the two electrolytes as observed for other sulfur electrochemical systems using electrolytes with varied electron donicity⁶⁷. A stronger bonding of Al₂(Se_n)₃ to the solvent (hence more stabilized) leads to higher change of Gibbs free energy of the discharge reaction, and thus a higher voltage. Also, as governed by the Nernst equation, the concentration of the Al₂(Se_n)₃ also impacts the potential of the redox reaction. We do note that as the two cells both show a single-plateau discharge profile, any large difference in the selenium speciation mechanism or dynamics can be excluded.



Extended Data Fig. 6 | Analysis of the basic components that comprise the Se K-edge X-ray absorption spectra during operando discharge at 170 °C.

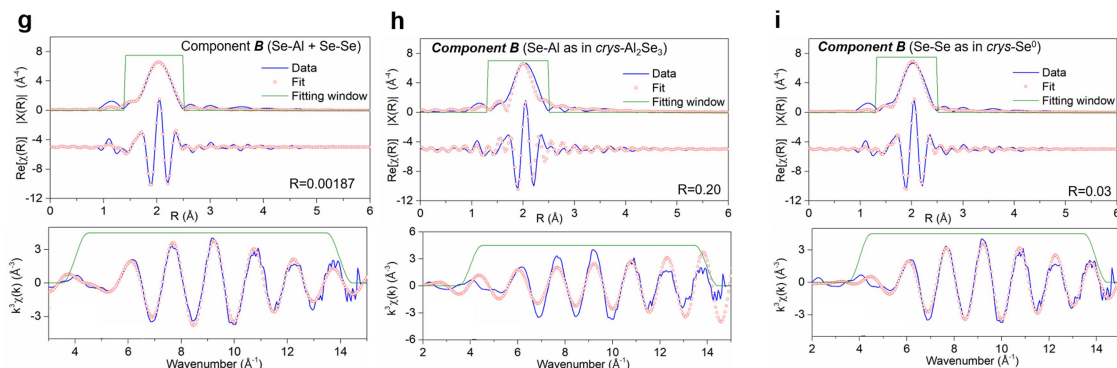
a, b, The XRD pattern (**a**) and SEM image (**b**) of the selenium composite used for XAFS measurement; the absence of diffraction peaks indicates the non-crystalline nature of Se. **c**, The magnified XANES spectra in a representative region that shows the isosbestic points shared by the first few but all not all spectra. **d, e**, The plots of logarithmic variance (**d**) and eigenvalue (**e**) of each component for the principal component analysis (PCA), showing that at least 3 components are required to capture > 99.99% of the XAFS data set. **f**, The plots of first five PCA-derived components (Components 3–5 magnified in the inset); while Components 1, 2, 3 show meaningful curvature, Component 4 and beyond start to lose significance. **g**, The k -space EXAFS $k^2\chi(k)$ oscillations of three identified basic components using MCR-ALS method, with the input data being either energy (E) space or frequency (k) space data sets. Notably, the **three** identified components are the same, irrespective of the

type of input data set, validating the utilized analysis procedure. **h–j**, Fitting results of the EXAFS data (top: magnitude and real-part of Fourier transforms of $k^3\chi(k)$; bottom: the corresponding $k^3\chi(k)$ oscillations) for the standard selenium Se⁰ measured at 170 °C (**h**) and crystalline Na₂Se₂ measured at 25 °C (**i**) and the summary of the fitting parameters (**j**). Na₂Se₂ was synthesized by reaction of Na-naphthalene with selenium (see Methods). The window in the FT panels is the fit range used and the window in the EXAFS panels is the k -space data range used for the FT. The paths used for fitting Na₂Se₂ are from the Se-Se and Se-Na coordinations calculated from the crystalline Na₂Se₂. The fitting of Se⁰ allows us to determine the amplitude reduction factor (S_0^2 : 0.973) which is a beam-related constant and is used for fitting all spectra collected in this study. The methodology of fitting the Na₂Se₂ standard validates taking multiple paths from crystalline data to fit the first (and second) Se shell of unknown spectra as will be shown below.



f

EXAFS spectra (panel#)	Paths	CN	R	σ^2	ΔE_0	R-factor	χ^2_{red}	Evaluation of fitting
Component A (a)	Se-Se	2.03(14)	2.376(4)	0.0054 (2)	-0.17 (99)	0.0040	292	Good fit
Component C (b)	Se-Al	2.93(20)	2.397(6)	0.0064 (8)	2.8 (0.9)	0.0036	112	Best fit
Attempted but inappropriate fits								
Component C (c)	Se-Na	9.2(1.3)	2.623 (12)	0.0084 (14)	-49 (2)	0.019	313	Too large ΔE_0 , large R-factor and χ^2_{red}
Component C (d)	Se-Cl	2.0(0.2)	2.348 (11)	0.0068 (13)	16.2 (1.3)	0.011	296	Too large ΔE_0 , large R-factor and χ^2_{red}
Component C (e)	Se-Al	3.0(0.6)	2.394 (20)	0.0064 (fixed)	1.7 (3.5)	0.004	323	Too low CN of Se-Cl (with large error), large χ^2_{red}
	Se-Cl	0.25(1.88)	2.098 (330)	0.018 (0.102)				



j

Component B panel#	Paths	CN	R	σ^2	ΔE_0	R-factor	χ^2_{red}	Evaluation of fitting
Ext. Fig. 7 (a)	Se-Al	0.96 (13)	2.492 (19)	0.0029 (36)	6.8 (3.2)	0.0027	192	Best fit
	Se-Se	2.30(32)	2.381 (15)	0.0067 (fixed)				
Attempted but inappropriate fits								
Ext. Fig. 7 (b)	Se-Al	0.6 (3)	2.324 (30)	-0.024 (2)	10.7 (6.7)	0.2	7990	Negative σ^2 and poor fit
Ext. Fig. 7 (c)	Se-Se	1.2 (3)	2.377 (14)	0.0044 (15)	-1.6 (3.7)	0.03	1406	Poor fit

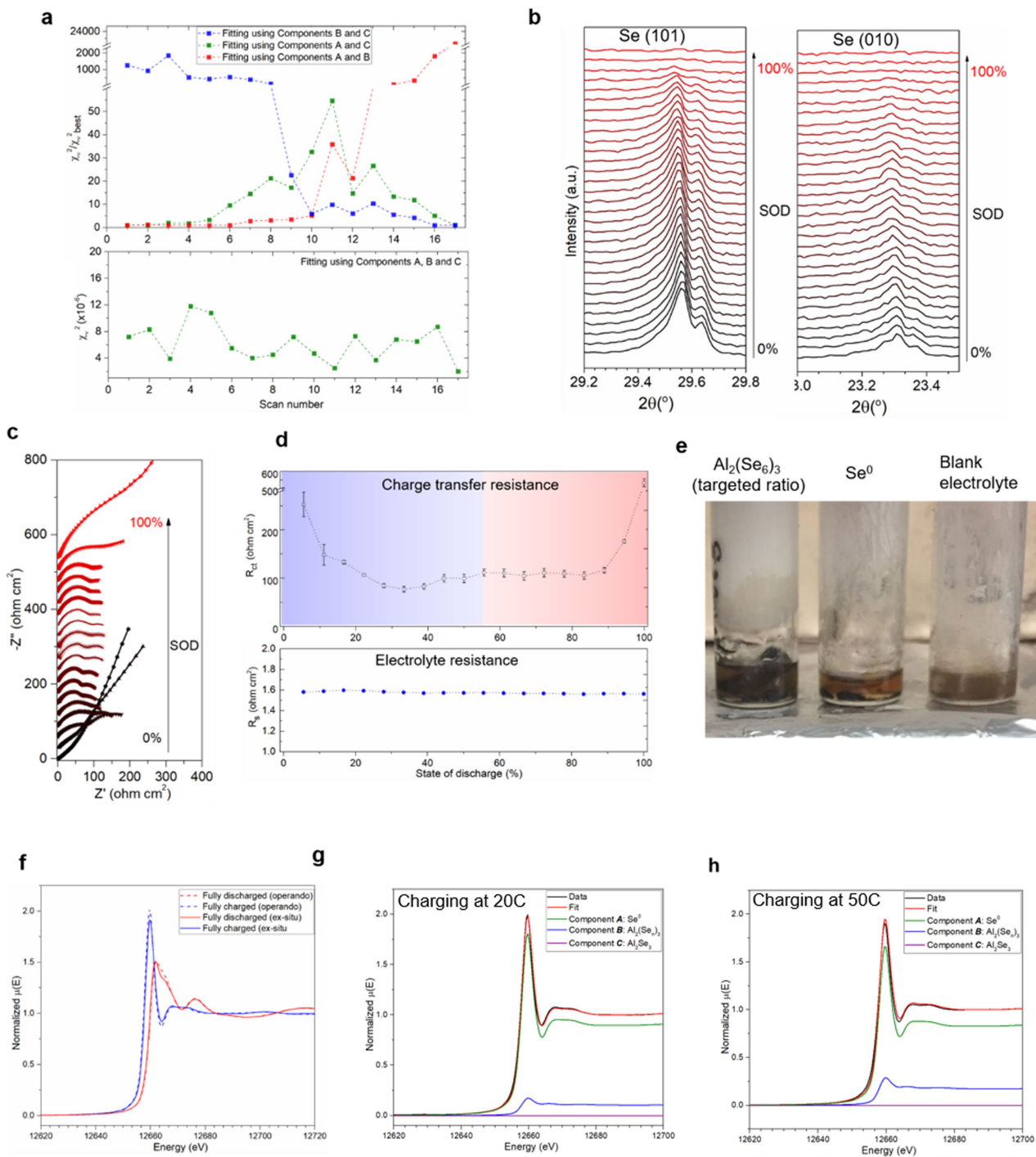
Extended Data Fig. 7 | See next page for caption.

Article

Extended Data Fig. 7 | The EXAFS fitting of the Se K-edge spectra of

Principal Components A and C. **a**, Component **A** is fit very well using Se-Se correlations, as in crystalline Se⁰ (P 3₁ 21). **b-e**, The fit for component **C** using different models and summary of the fitting parameters (**f**). The top of each panel is the magnitude and real-part of Fourier transforms (FT) of $k^3\chi(k)$, and the bottom is the corresponding $k^3\chi(k)$ oscillation. The window in the FT panels is the fit range used and the window in the EXAFS panels is the k -space data range used for the FT. The fitting R-range is from 1.3 to 2.5 Å, except that when the longer Se-Na path is included, the R-range is increased from 1.3 to 3 Å. All

fits were carried out in R-space. Evaluation of the various fits shows that the Component **C** is best modelled by using selenium-aluminium correlation exclusively (fit **b**). **g-i**, The attempted EXAFS fitting for component **B** using just one path: Se-Se (**a**) or Se-Al (**b**), and summary of the fitting parameters (**c**). Evaluation of all attempted fits shows that Component **B** is best modelled by using both Se-Al and Se-Se correlations. Importantly, we note that the R of Se-Al in Component **B** is different from that in Component **C** (2.494 vs. 2.397 Å), proving that Component **B** is distinguished from Component **C** and is thus indeed a necessary component.

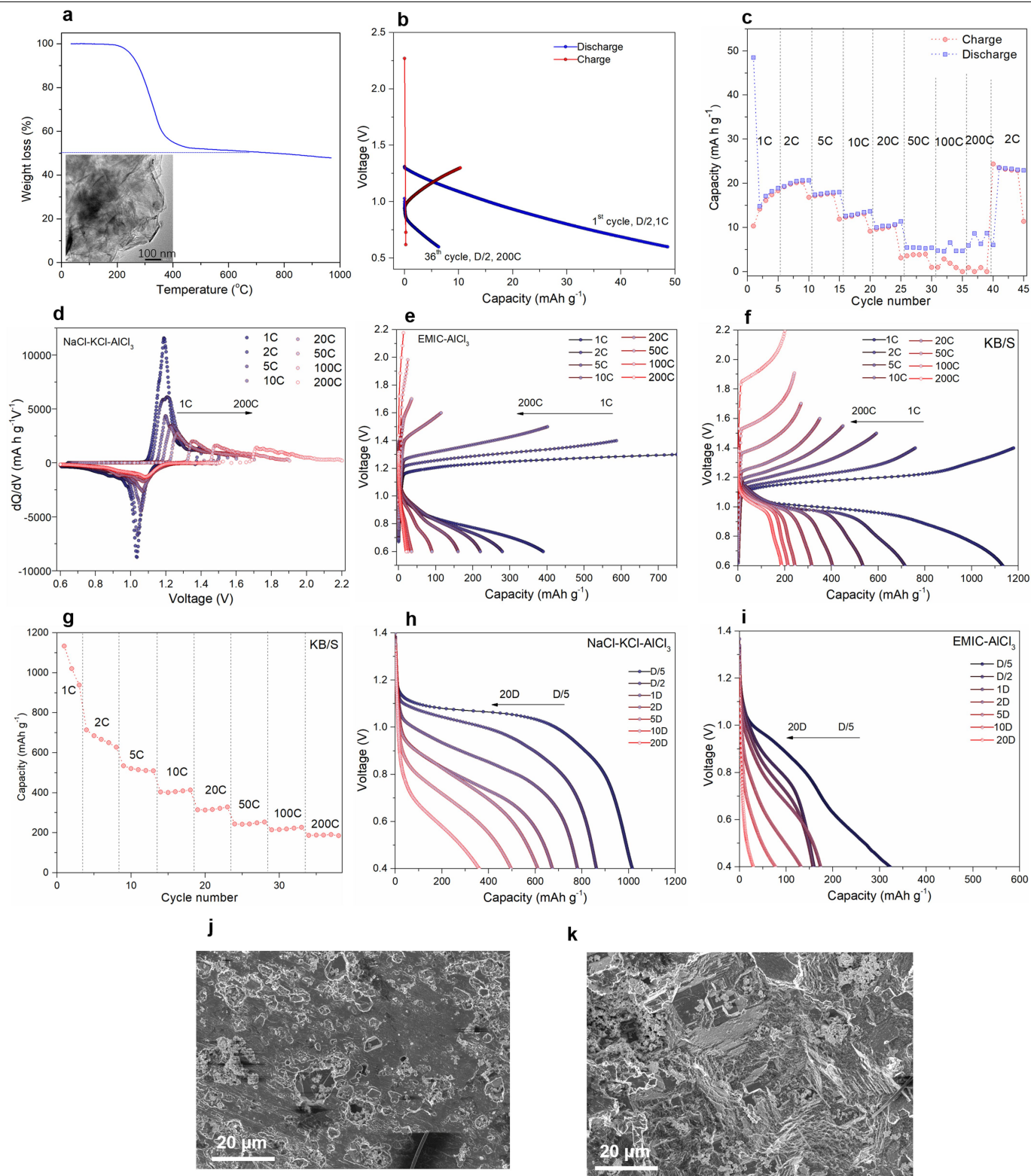


Extended Data Fig. 8 | See next page for caption.

Article

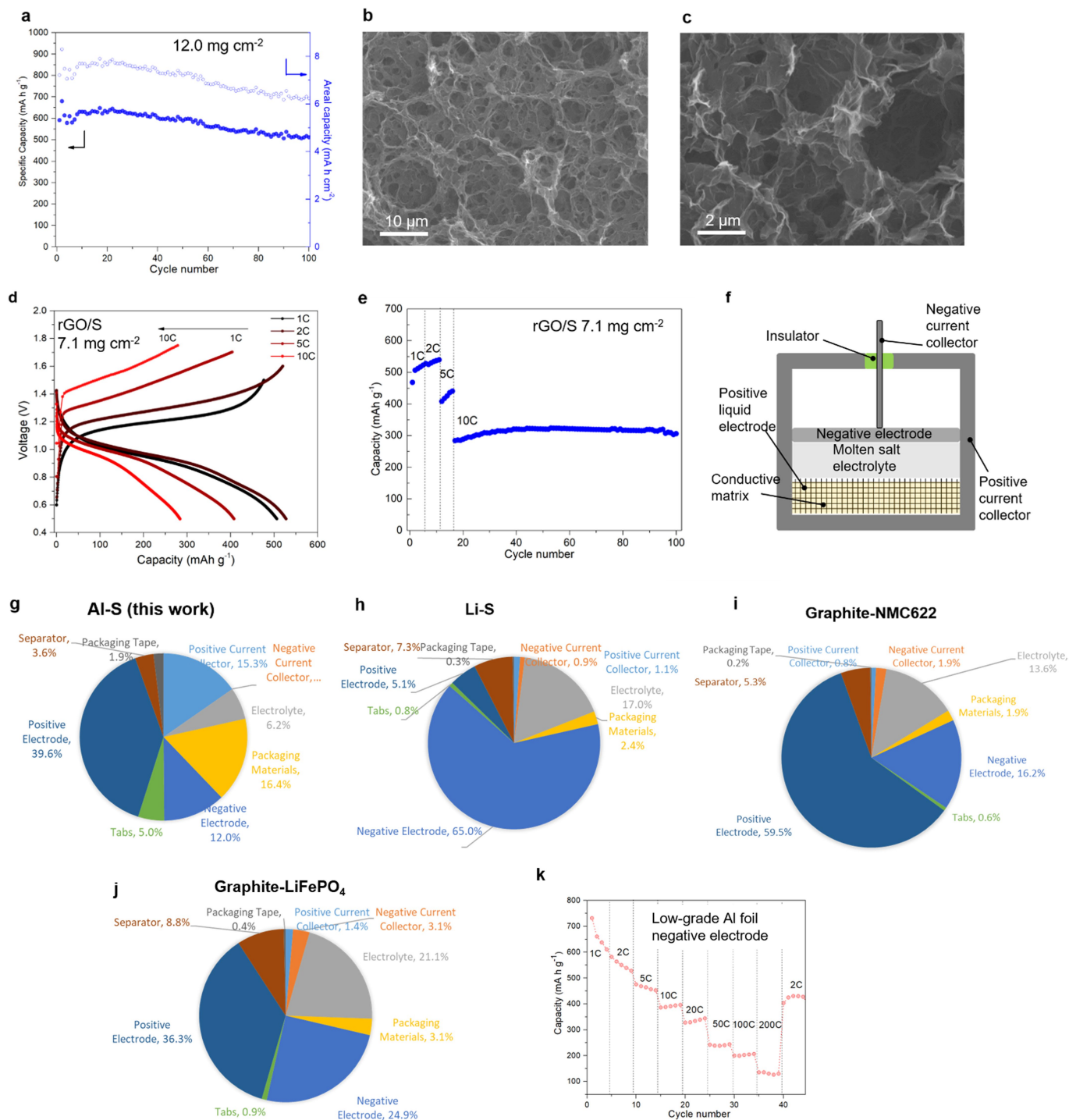
Extended Data Fig. 8 | Further analysis of the reaction mechanism on discharge of Al-Se cells fitted with molten NaCl-AlCl₃ electrolyte. a, The χ_{red}^2 of linear combination fittings using three components ($\chi_{red}^2_{best}$, bottom) and using only two of the three components (ratio over $\chi_{red}^2_{best}$, top). The significantly higher χ_{red}^2 using only two components proves that three components are necessary to capture the information of the entire data set; the almost constant $\chi_{red}^2_{best}$ across all scans indicates further that 3 components faithfully reproduce the entire data set, in complete agreement with the PCA analysis (Extended Data Fig. 6d, e). More importantly, the low χ_{red}^2 of using Components **A** and **B** for scans 1–6 ($\chi_{red}^2/\chi_{red}^2_{best} - 1$) indicates that only **A** and **B** are present in these 6 scans, and similarly, the high χ_{red}^2 of using **B** and **C** for scans 10–15 ($\chi_{red}^2/\chi_{red}^2_{best} = 4-11$) indicates that **A** is necessary and present in these scans. **b,** The *operando* X-ray diffraction patterns of the crystalline Se cathode during discharge at D/10 and 180 °C, featuring the Se (101) and Se (010) peaks. The Se peaks do not disappear until the end of discharge. **c, d,** Nyquist plots of the *in-situ* measured impedance data on an Al|Se cell, as a function of the state of discharge (SOD) from bottom to top (**c**); the evolution of charge transfer resistance (R_{ct}) and electrolyte resistance (R_s) of the cell, as fitted from the Nyquist plots (**d**). For consistency amongst all impedance data, circle fitting of the Nyquist plots on the high-frequency semicircle was performed (instead of finding one equivalent circuit for all), and the first intercept (of the fitted circle with the real-axis) is regarded as R_s and the distance between the two intercepts is regarded as R_{ct} . The error bars are the standard deviations based on three measurements at the corresponding SOD. The R_s remains constant at around 1.5 ohm cm² for all SOD, indicating there is minimal change of the electrolyte composition and dissolution of formed species. The R_{ct}

experiences initial decrease (SOD: 0–30%, due to formation of partially soluble Al₂(Se_n)₃ species), slight increase (SOD: 30–55%, probably due to initial formation of Al₂Se₃), stabilization (SOD: 55–85%), and eventual increase (SOD: 85–100%, eventual formation of Al₂Se₃). This is consistent with the trend in the proposed reaction mechanism in Fig. 3e. **e,** The picture of Al₂(Se_n)₃ (targeted stoichiometry) and selenium in the molten NaCl-AlCl₃ electrolyte placed on a hot plate (around 180 °C); partial solubility is confirmed by the darkened color. The nominal Al₂(Se_n)₃ was prepared by mixing the targeted amount of Se and Al₂Se₃ in the melt; thus, it may not reflect the exact ratio and serves only as demonstration of partial solubility of such compounds. Note that elemental selenium appears to have some solubility as well. **f-h,** the *ex-situ* XAFS studies on the fast-charged selenium electrodes: the XAFS spectra of fully discharged and charged electrodes collected *operando* and *ex-situ* for comparison (**f**); as the fast-charging study has to be performed *ex-situ* due to the limited time resolution of the XAS scan (-10 min), the very similar XAFS features using two measurement approaches indicates that the chemical states of selenium species remain unchanged if we stop and cool down the warm cell at a certain SOC (the electrolyte freezes). The *ex-situ* Se K-edge XAFS spectra of the selenium electrodes charged at 20C (**g**) and 50C (**h**) respectively; the spectra were collected using transmission mode on the retrieved fast charged electrode, and fitted by linear combination fittings using the three principal components. By quantifying the components using linear combination fitting, we observed that the cathode recharged at 20C contains 10.5% of the Al₂(Se_n)₃ and 89.5% of Se⁰, and the one recharged at 50C contains 17.3% of the Al₂(Se_n)₃ and 82.7% of Se⁰. No component C was observed in both electrodes.



Extended Data Fig. 9 | The electrochemical behaviour of Al-S cells fitted with molten chloroaluminate electrolytes. a, The TGA plot and the representative TEM image of the S/graphene composite, which contains 50 wt% of sulfur. **b**, **c** The first-cycle voltage-time trace (**b**) and capacity retention (**c**) of the graphene that is used to prepare the sulfur composite. Capacity retention was measured at various charging rates and at constant discharge rate of D/2. **d**, the differential capacity plot (dQ/dV) of the Al-S cell in molten NaCl-KCl-AlCl₃ at different rates at 110 °C. **e**, Voltage-time traces of an Al-S cell in EMIC-AlCl₃ at different rates at 110 °C. **f**, Capacity retention (discharge

capacity, **f**) and the corresponding voltage-time traces (**g**) of an Al-S cell using KB/S composite in NaCl-KCl-AlCl₃ at 110 °C, at constant discharge rate of D/2. **h**, **i**, The discharge voltage-time traces of Al-S cells in NaCl-KCl-AlCl₃ (**h**) and EMIC-AlCl₃ (**i**), at various discharge rates (D/5 to 20D) and at constant charge rate of C/2. **j**, **k**, Two representative surface SEM images of the Al negative electrode in Al-S cells after the charging rate-capability measurement. The electrode was thoroughly washed by acetonitrile in the glovebox before imaging.



Extended Data Fig. 10 | The practical attributes of Al-S batteries fitted with molten alkali chloroaluminate electrolyte. **a**, The discharge capacity retention (specific capacity and areal capacity) of an Al-S cell using sulfur electrodes with 12.0 mg cm⁻² areal loading in molten NaCl-KCl-Cl₃ at a D/5 and C/5 rate. **b-e**, The representative SEM images of the prepared 3D interconnected reduced graphene oxide/sulfur composite (rGO/S) (**b-c**), and the voltage-time traces (**d**) and charging rate capability at constant discharge rate of D/2 (**e**) using rGO-S electrode with an areal sulfur loading of 7.1 mg cm⁻². **f**, A schematic illustration of the proposed tri-layer structure of a large-scale Al-S battery that is modified from the architecture of the liquid metal battery. **g-j**, the cost breakdown of the representative cell chemistry (Al-S battery, Li-S, graphite-NMC622 and graphite-LiFePO₄); the cost of electrodes includes the associated carbon and binder where applicable; and the percentage is rounded up to integral digit (the details of calculation is shown in Extended Data Table 1). **k**, The fast-charge performance of an Al-S battery fitted with a low-grade (food

packaging foil) Al-foil negative electrode, foretelling major cost reduction. Our current use of Mo current collector is for proof-of-concept demonstration of the Al-S battery using alkali chloroaluminate melt, and Mo foil is not an ideal positive current collector for a practical battery. Modifications can be Mo coated Al foil (Mo coating by vapor deposition: 300-550 nm thick)⁶⁸, TiN coated Al foil (TiN coating by pulsed DC plasma enhanced CVD)^{69,70}, or non-graphitic carbon foil. In our estimate calculation, the model of Mo coated Al foil (Mo: 0.5 μm thick) was used. Therefore, on the package level, our Al-S battery is expected to cost about 1/4 and 1/5 that of the graphite-LiFePO₄ and graphite-NMC622 battery (20.8 vs 80.3 and 94.7 USD\$ kWh⁻¹; unit price of each material/component is based on the latest market and as accurate as possible). As the price is the latest market price or the projected price when market price is unavailable, the cost may fluctuate and contain errors, and we do expect further modifications when it comes to the manufacturing. Nevertheless, we believe that this chemistry offers a great economical advantage.

Extended Data Table 1 | The data for the calculation of cell-level energy density and cost for the Al-chalcogen batteries in comparison with other cutting-edge and commercial battery systems by assuming a 065070 pouch cell geometry, mainly collected from the literature and/or based on market price⁷¹⁻⁷⁴

Parameters	Units	Al-S	Al-Se	Li-S	Graphite-NMC622	Graphite-LiFePO ₄	Graphite-NCA	Al-S (EIMC)	
Positive Electrode (PE)	PE AM ^[1]	S	Se	S	NMC622	LiFePO ₄	NCA	S	
	PE AM capacity	mAh g ⁻¹	1200	670	1200	180	145	200	1200
	PE AM density	g cm ⁻³	2.07	4.82	2.07	4.8	3.6	4.8	2.07
	PE carbon additives		Super P [®]						
	PE binder ^[2]		PVDF						
	AM: carbon: binder ^[3]	wt/wt	75:20:5	85:10:5	75:20:5	95:2.5:2.5	96:2:2	95:2.5:2.5	75:20:5
	PE CC ^[4]		Mo@Al	Mo@Al	Al	Al	Al	Al	Mo@Al
	PE areal loading	mgcm ⁻²	10	10	10	22	25	22	10
	PE compacted density ^[5]	g cm ⁻³	1.2	3.5	1.2	3.2	2.2	3.2	1.2
	PE porosity		0.43	0.32	0.43	0.31	0.37	0.31	0.43
PE thickness	μm	95	45	95	80	125	80	95	
Number of PE layers in pouch		34	50	27	25	26	25	34	
Negative Electrode (NE)	NE AM ^[6]	Al metal	Al metal	Li metal	Graphite	Graphite	Graphite	Al metal	
	NE AM capacity	mAh g ⁻¹	2981	2981	3861	365	365	365	2981
	NE AM density	g cm ⁻³	2.7	2.7	0.534	2.3	2.3	2.3	2.7
	NE carbon additives		N/A	N/A	N/A	Activated carbon	Activated carbon	Activated carbon	N/A
	NE binder ^[7]		N/A	N/A	N/A	SBR-CMC	SBR-CMC	SBR-CMC	N/A
	AM: carbon: binder ^[8]	wt/wt	100:0:0	100:0:0	100:0:0	95.5 : 1: 3.5	95.5 : 1: 3.5	95.5 : 1: 3.5	100:0:0
	NE CC		Al foil	Al foil	Cu foil	Cu foil	Cu foil	Cu foil	Al foil
	NE areal loading	mgcm ⁻²	3.6	2.3	3.1	11.8	11.0	13.2	3.6
	NE compacted density ^[9]	g cm ⁻³	2.7	2.7	0.534	1.55	1.55	1.55	2.7
	NE porosity		0	0	0	0.32	0.32	0.32	0
NE thickness	μm	19.5	14.5	63.6	82.5	76.8	91.1	21.2	
Number of NE layers in pouch		35	51	28	26	27	26	35	
N/P ratio ^[10]		1.2	1.2	1.4	1.1	1.1	1.1	1.2	
Electrolyte	Electrolyte materials ^[11]	NaCl-KCl-AlCl ₃	NaCl-AlCl ₃	LiTFSI/DOL+DME	LiPF ₆ /DMC+EC	LiPF ₆ /DMC+EC	LiPF ₆ /DMC+EC	EIMC- AlCl ₃	
	Electrolyte density ^[12]	g cm ⁻³	1.70	1.70	1.10	1.25	1.25	1.25	
	Electrolyte amount	g	10.3	12.3	6.7	6.8	6.6	7.6	11.7
	Electrolyte calculation ^[13]		Void*0.8	Void*0.8	Void*0.8	2.5 g/Ah	2.5 g/Ah	2.5 g/Ah	Void*0.8
Separator	Separator materials	Glass fiber	Glass Fiber	Polyolefin	Polyolefin	Polyolefin	Polyolefin	Glass Fidr	
	Separator porosity		0.5	0.5	0.45	0.45	0.45	0.5	
	Separator thickness		20	20	16	16	16	20	
Cell geometry	Size of pouch	mm	50*70*6 (Width * Height * Thickness)						
	Size of PE	mm	45* 65 (Width * Height)						
	Size of NE	mm	47*67 (Width * Height)						
	PE CC thickness	μm	12						
	NE CC thickness	μm	6						
	Size of PE tab	mm	10*15 (Width * Height)						
	Size of NE tab	mm	10*13 (Width * Height)						
	Size of outer tab	mm	10*28*0.1 (Width * Height * Thickness)						
Packaging film		Aluminum-plastic film:0.153 thick; density: 21.8 mg/cm ² ; margin of 5 mm							
Cell	Cell capacity	mAh	8950	8328	6844	2751	2646	3056	8950
	Voltage	V	1.08	0.88	2.1	3.8	3.3	3.7	0.45
	Energy density	Wh L⁻¹	503	405	748	561	380	580	209
Price and cell cost	PE AM	\$ kg ⁻¹	0.22	57.0	0.22	29.2	8.7	34.0	0.22
	NE AM	\$ kg ⁻¹	4.1	4.1	153.8	12.3	12.3	12.3	4.1
	PE CC	\$ kg ⁻¹	10.0	10.0	4.1	4.1	4.1	4.1	10
	NE CC	\$ kg ⁻¹	4.1	4.1	20.0	20.0	20.0	20.0	4.1
	Electrolyte	\$ kg ⁻¹	0.5 ^[14]	0.5	15.4	15.4	15.4	15.4	100.0
	Separator	\$ m ⁻²	0.03 ^[15]	0.03	0.54	0.54	0.54	0.54	0.03
	Activated carbon	\$ kg ⁻¹	6.9						
	PVDF	\$ kg ⁻¹	38.5						
	SBR-CMC	\$ kg ⁻¹	40.9						
	Outer tab	\$	0.05 (tab glue included)						
	Packaging tape	\$	0.0038 (5.4 \$ m ⁻²)						
	Packaging film	\$ m ⁻²	0.04 (3.85 \$ m ⁻²)						
	Cell Cost	\$/kWh	20.8	127.8		59.5	94.7	80.3	96.3

See next page for footnote.

Article

Notes: [1] PE=Positive electrode, AM= active materials;

[2] PVDF: polyvinylidene fluoride;

[3] the weight ratio of active material: activated carbon: binder in weight percent;

[4] CC: Current collector;

[5] The projected electrode compacted density after calendaring and drying;

[6] NE=Negative electrode, AM= active materials;

[7] SBR: Styrene-butadiene rubber; CMC: carboxymethyl cellulose;

[8] For the Al and Li metal electrodes, no binder or additive is involved;

[9] The projected electrode compacted density after calendaring and drying;

[10] The negative/positive electrode capacity ratio;

[11] LiTFSI/DOL+DME: 1M lithium bis(trifluoromethanesulfonyl)imide in mixed solvent of dioxolane + dimethyl ethane; LiPF₆/DMC+EC: 1M LiPF₆ in the mixed solvent of dimethyl carbonate and ethylene carbonate

[12] The density of the KCl-NaCl-AlCl₃ and EMIC-AlCl₃ is set to 1.7 and 1.5g/ml, respectively based on literature values^{75,76}.

[13] The electrolyte volumes in sulfur/selenium batteries are calculated as 80% of the total void space in the pouch (electrode porosity, separator porosity and extra space in the pouch); the electrolyte volumes of lithium-ion batteries are calculated as 2.5g Ah⁻¹ based on empirical parameters.

[13] NaCl: 0.04 \$ kg⁻¹; KCl:0.22 \$ kg⁻¹; AlCl₃:0.65 \$ kg⁻¹.

[14] The glass fiber price is projected based on current glass fiber industry market.